Editors' Suggestion

Strong-coupling topological states and phase transitions in helical trilayer graphene

Yves H. Kwan,[1] Patrick J. Ledwith,[2] Chiu Fan Bowen Lo,[2] and Trithep Devakul[3,4]
[1]*Princeton Center for Theoretical Science, Princeton University, Princeton, New Jersey 08544, USA*
[2]*Department of Physics, Harvard University, Cambridge, Massachusetts 02138, USA*
[3]*Department of Physics, Stanford University, Stanford, California 94305, USA*
[4]*Department of Physics, Massachusetts Institute of Technology, Cambridge, Massachusetts 02139, USA*

(Received 26 September 2023; revised 13 February 2024; accepted 16 February 2024; published 21 March 2024)

Magic-angle helical trilayer graphene relaxes into commensurate moiré domains, whose topological and well-isolated sets of narrow bands possess ideal characteristics for realizing robust correlated topological phases, compared with other graphene-based moiré heterostructures. Combining strong-coupling analysis and Hartree-Fock calculations, we investigate the ground states at integer fillings ν, and uncover a rich phase diagram of correlated insulators tuned by an external displacement field D. For small D, the system realizes several competing families of symmetry-broken generalized flavor ferromagnets, which exhibit various anomalous Hall signatures and Chern numbers as high as $|C| = 6$. The interaction-induced dispersion renormalization is weak, so that the band flatness and the validity of strong-coupling theory are maintained at all integer fillings. For experimentally accessible displacement fields, the strong-coupling insulators at all ν undergo topological phase transitions, which appear continuous or weakly first order. For larger D, we also find translation symmetry-broken phases such as Kekulé spiral order. Our results demonstrate the robust capability of helical trilayer graphene to host gate-tunable topological and symmetry-broken correlated phases, and lay the groundwork for future theoretical studies on other aspects such as fractional topological states.

DOI: 10.1103/PhysRevB.109.125141

I. INTRODUCTION

The coexistence of narrow bands, electronic topology, and strong interactions provides a fertile ground for realizing fascinating quantum phases of matter. A now-classic example is realized by the fractional quantum Hall effect in two-dimensional (2D) semiconductor quantum wells [1], where the requisite conditions are generated by the Landau quantization induced by an external magnetic field. The presence of flavor degrees of freedom, like spin, valley, layer, or orbital components, further enriches the physics, even at integer fillings, where spontaneous symmetry breaking introduces new collective phenomena such as topological defects and additional quantized responses [2]. Various platforms have been shown to experimentally realize such quantum Hall ferromagnetism (QHFM), such as quantum Hall bilayers [3] and the zeroth Landau level of graphene [4]. These systems are also typically associated with an enlarged manifold of nearly degenerate orders.

Magic-angle twisted bilayer graphene (TBG) [5–8] has attracted remarkable attention as the poster child of the family of correlated moiré materials [9,10], and has accumulated an ever-growing catalog of experimentally observed phenomena. Theoretically, this system holds promise for possessing all of the above ingredients without the need for an external magnetic field. The spatially modulated interlayer tunneling is responsible for the small dispersion, the Dirac points imbue the moiré bands with nontrivial topology, and the graphene layers supply the valley, spin, and sublattice degrees of freedom. This notion of interactions dominating a set of narrow topological bands in TBG is formalized in the "strong-coupling" framework [11–13], which enables a controlled analysis of various deviations from an idealized solvable limit with completely flatbands and enhanced symmetries [14]. The result is a manifold of closely competing symmetry-broken correlated insulating states, akin to generalized QHFM. However, while predicted to arise at various fillings in the strong-coupling limit, such topological states are often overpowered by competing nontopological states in TBG under realistic conditions. Part of the reason is due to the large interaction-induced "Hartree" dispersion at finite density [15–21], which originates from the real-space inhomogeneity of the moiré wave functions. This drives the system away from the strong-coupling regime, especially in the presence of strain [22–30], with the consequence being that an applied magnetic field or substrate alignment is often necessary to stabilize such topological states [21,31–41].

Recently, correlated topological states have been proposed to arise in helical trilayer graphene (HTG), a structure consisting of three graphene layers with identical twist angles θ between adjacent layers [42] (see also Refs. [43–51]). In the absence of lattice relaxation, the pairs of adjacent layers in HTG form two moiré lattices, which themselves form a supermoiré lattice at very long length scales ($a_{mm} \simeq 250\,\text{nm}$ near $\theta \simeq 1.8^\circ$). Theoretical analysis demonstrated that lattice relaxation plays a key role and leads to the formation of a commensurate single-moiré structure (with moiré periodicity $a_m \simeq 8\,\text{nm}$) over large regions, made possible by the slight elastic deformation of the graphene layers [42,48]. These commensurate regions come in two C_{2z}-related

 ©2024 American Physical Society

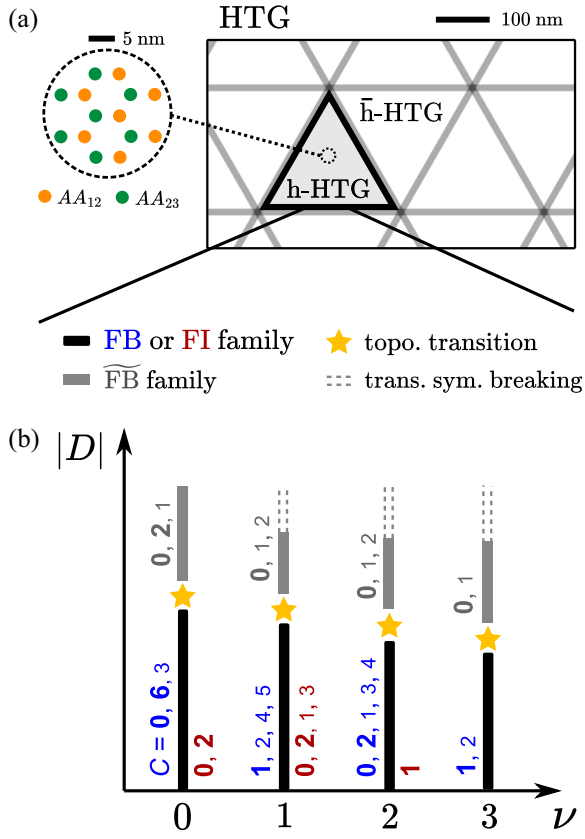

FIG. 1. Summary of correlated insulating phases in h-HTG at integer fillings ν as a function of displacement field D. (a) The supermoiré structure of helical trilayer graphene (HTG) relaxes into large moiré-periodic domains of h-HTG and h̄-HTG separated by gapless domain walls (gray). h-HTG realizes a honeycomb lattice consisting of AA stacking regions of the two pairs of adjacent layers. (b) Schematic phase diagram of h-HTG. At small D, there are two competing strong-coupling families of low-lying states, flavor balanced (FB, blue) and flavor imbalanced (FI, red), defined in Sec. III. They are characterized by a preference towards partial or full occupation of flavors respectively. The possible Chern numbers $|C|$ are shown, with large bold entries corresponding to the primary ground states predicted by our analysis. At a displacement field-tuned topological transition (stars), the system enters the F̃B phase whose set of Chern numbers differs from the zero-field case. At even higher fields, the system further realizes various translation symmetry-breaking phases (dotted lines).

versions, called h-HTG and h̄-HTG, which are tiled together and separated by a triangular network of narrow gapless domain walls (see Fig. 1). In the resulting structure of h-HTG, the AA regions of the two moiré lattices come together to form a moiré-scale honeycomb configuration. Henceforth, we focus on the physics of commensurate h-HTG, though our results straightforwardly generalize to h̄-HTG as well.

The most remarkable aspect of h-HTG lies in its electronic properties. The single particle electronic structure in each spin and valley sector consists of a pair of flat topological bands with Chern numbers $|C| = 1, 2$ and near-ideal quantum geometry. Because the relaxed structure breaks C_{2z} symmetry, the flatbands carry nonzero total valley Chern number. Furthermore, the flatband manifold is isolated from remote bands by a significant energy gap $E_{\text{rem. gap}} \simeq 100\,\text{meV}$, much larger than the interaction energy scale. These features suggest that h-HTG is an ideal platform for exploring interaction-dominated physics in topological bands, with potential for realizing exotic topological states such as integer and fractional Chern insulators at zero magnetic field. These findings call for a detailed theoretical study of the interaction-driven physics.

In this paper, we perform a comprehensive analysis of the interacting phase diagram of h-HTG at integer fillings. We employ self-consistent Hartree-Fock (HF) mean-field theory and strong-coupling analysis, which reveals a rich phase structure that is highly dependent on an externally applied displacement field. For weak displacement fields, we uncover a plethora of closely competing symmetry-broken topological states with Chern numbers as high as $|C| = 6$ (see Fig. 1), which are well captured within strong-coupling perturbation theory. We find that, compared to other graphene-based moiré systems, the Hartree corrections are weak owing to the relatively homogeneous charge density of the central-band wave functions. This maintains the stability of strong-coupling correlated insulators at nonzero integer fillings, safeguards against mixing with remote bands, and allows for relatively flat quasiparticle bands even when accounting for interaction renormalization.

For critical displacement fields well within experimental capabilities, our calculations show that all integer filling factors can undergo continuous or weakly first-order topological phase transitions to states with smaller or vanishing Chern numbers (see schematic of Fig. 1). Interestingly, the states just above the transition still preserve significant strong-coupling character, in that they retain sizable flavor and/or sublattice polarizations close to the zero-field case. This is possible because the transition involves a band inversion that is localized in momentum space. Hence, h-HTG potentially realizes the universal theory of Dirac mass inversion in the strongly interacting regime, away from weak-coupling one where it is normally studied. Importantly, such physics is experimentally accessible by tuning the displacement field.

For yet larger fields, we find translation-symmetry-breaking (TSB) phases such as charge density waves (CDWs), as well as a Kekulé spiral order [28–30] that has connections to that recently imaged in TBG [26] and mirror-symmetric trilayer graphene [52] (which differs from HTG in that it has alternating twists between the layers).

Our results highlight HTG as a highly tunable system that exhibits a panoply of orbital Chern insulators, symmetry-breaking orders, and displacement field-tuned topological transitions. The phenomena uncovered in this paper can be studied experimentally through various probes. From a theoretical standpoint, we argue that h-HTG presents a near-ideal moiré platform for quantum-Hall-like strong-coupling physics, including more exotic phases like fractional Chern insulators [53–61], and is relatively free from the various complications that are present in other related systems. We also discuss various extensions such as noninteger fillings, and the impact of the supermoiré structure of domains in HTG.

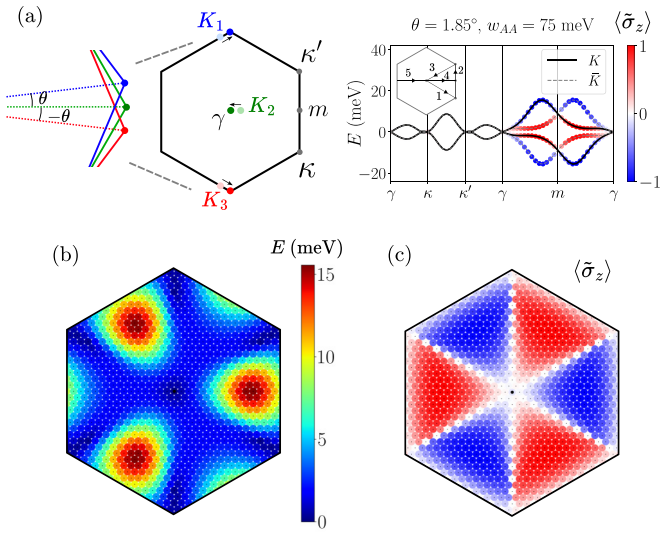

FIG. 2. Noninteracting band structure at zero displacement field. (a) Left: The moiré Brillouin zone (mBZ) is determined from the Dirac momenta of the three layers, which relax slightly (arrows) to form a locally commensurate structure. Right: Dispersion of the central bands along a path in the mBZ shown in the inset. Color indicates polarization in the Chern-sublattice basis $\langle\tilde{\sigma}_z\rangle$, where $\tilde{\sigma}_z = +1(-1)$ is sublattice A (B). (b), (c) Energy dispersion and Chern-sublattice polarization of the K-valley conduction band in the mBZ. The color scale in (c) is the same as in (a).

II. MODEL AND METHODS

A. Noninteracting continuum model

Our starting point for studying h-HTG is a generalization of the Bistritzer-MacDonald (BM) continuum model for valley K ($\tau = +$) [42,62]:

$$H_K^{\mathrm{BM}} = \begin{bmatrix} -iv_F\boldsymbol{\sigma}\cdot\nabla & T(\boldsymbol{r}-\boldsymbol{d}_t) & 0 \\ T^\dagger(\boldsymbol{r}-\boldsymbol{d}_t) & -iv_F\boldsymbol{\sigma}\cdot\nabla & T(\boldsymbol{r}-\boldsymbol{d}_b) \\ 0 & T^\dagger(\boldsymbol{r}-\boldsymbol{d}_b) & -iv_F\boldsymbol{\sigma}\cdot\nabla \end{bmatrix} \quad (1)$$

where the matrix acts on layer space $l = 1, 2, 3$, $\boldsymbol{\sigma} = (\sigma_x, \sigma_y)$ acts on the microscopic sublattice, and the graphene Dirac velocity $v_F = 8.8\times10^5\,\mathrm{ms}^{-1}$ [62]. The Hamiltonian for valley $\bar{K}$ ($\tau = -$) can be found by time reversal. Combined with spin $s = \uparrow, \downarrow$, there are four spin-valley flavors. Note that Eq. (1) has been written in a layer-boosted frame such that a Bloch function at momentum $\boldsymbol{k}$ satisfies $\psi_{\boldsymbol{k},l}(\boldsymbol{r}+\boldsymbol{a}_i) = e^{i(\boldsymbol{k}-\boldsymbol{K}_l)\cdot\boldsymbol{a}_i}\psi_{\boldsymbol{k},l}(\boldsymbol{r})$, where $\boldsymbol{K}_l$ is the layer-dependent Dirac momentum, suitably deformed to allow for a commensurate structure. $\boldsymbol{K}_2$ folds onto the moiré γ point, while $\boldsymbol{K}_1$ ($\boldsymbol{K}_3$) folds onto κ (κ') [Fig. 2(a)]. $\boldsymbol{a}_i$ is a basis moiré lattice vector $\boldsymbol{a}_{1,2} = \frac{4\pi}{3k_\theta}(\pm\frac{\sqrt{3}}{2}, \frac{1}{2})$, where $k_\theta = 2K_D\sin\frac{\theta}{2}$, with K_D the Dirac wave vector.

The interlayer tunneling takes the form

$$T(\boldsymbol{r}) = \begin{bmatrix} w_{AA}t_0(\boldsymbol{r}) & w_{AB}t_{-1}(\boldsymbol{r}) \\ w_{AB}t_1(\boldsymbol{r}) & w_{AA}t_0(\boldsymbol{r}) \end{bmatrix},$$

$$t_\alpha(\boldsymbol{r}) = \sum_{n=0}^{2} e^{\frac{2\pi i}{3}n\alpha}e^{-i\boldsymbol{q}_n\cdot\boldsymbol{r}}, \quad (2)$$

$$q_{n,x} + iq_{n,y} = -ik_\theta e^{\frac{2\pi i}{3}n},$$

where $\boldsymbol{K}_{1,3} = \mp\boldsymbol{q}_0 + \boldsymbol{K}_2$. Lattice relaxation [63,64] and renormalization [65] effects lead to a suppression of the chiral ratio $\kappa = \frac{w_{AA}}{w_{AB}} < 1$, whose precise value is difficult to pin down. We fix $w_{AB} = 110\,\mathrm{meV}$ [62], but allow w_{AA} to vary. For most calculations, we set the chiral ratio to a physically reasonable value $\kappa \simeq 0.7$ [36,63–70]. The relative interlayer moiré shift corresponding to the structure of h-HTG is given by $\boldsymbol{d}_t - \boldsymbol{d}_b = \boldsymbol{\delta} = \frac{1}{3}(\boldsymbol{a}_2 - \boldsymbol{a}_1)$.

To model the effect of a displacement field D, which is tunable in dual-gated samples, we add an interlayer potential U to Eq. (1), such that layers $l = 1, 2, 3$ have energy shifts $+U, 0, -U$. The relation between the two is $U = d_{\mathrm{inter}}D/\epsilon_\perp$, where $d_{\mathrm{inter}} = 3.3\,\text{Å}$ is the interlayer distance and $\epsilon_\perp$ is the perpendicular dielectric constant (up to electrostatic corrections which must be taken into account self-consistently [71]). The largest displacement fields attainable in experiment around charge neutrality are $D/\epsilon_0 \approx 1\,\mathrm{V/nm}$, which corresponds to $U \approx 80\,\mathrm{meV}$ assuming $\epsilon_\perp \simeq 4$. We only consider positive U since negative values are related by symmetry.

As shown in Figs. 2(a) and 2(b) for $U = 0$, the central noninteracting BM bands (two per flavor) become narrow with bandwidth $W \approx 20\,\mathrm{meV}$ near the magic angle $\theta \approx 1.8°$. Since the remote band gaps are large $\approx$100 meV, we project the system into the central bands. The topology of the bands is manifest in the Chern basis (also called the sublattice basis), obtained by diagonalizing the microscopic sublattice operator σ_z within this subspace [11–13,72]. We introduce a Chern-sublattice label $\tilde{\sigma}_z = A, B$ according to the predominant microscopic sublattice polarization. Unless otherwise stated, the term "sublattice" refers directly to this label rather than the microscopic sublattice polarization. The Chern bands can be therefore indexed by $(\tau, s, \tilde{\sigma})$, with Chern numbers [42]

$$C_{K,s,A} = 1, \quad C_{K,s,B} = -2,$$
$$C_{\bar{K},s,A} = -1, \quad C_{\bar{K},s,B} = 2. \quad (3)$$

The most dispersive parts of the BM bands, which lie along the γ-m lines in the moiré Brillouin zone (mBZ), predominantly arise from the B sublattice [Figs. 2(b) and 2(c)]. Meanwhile, the kinetic energy of Bloch states dominated by the A sublattice remains small. Note that the microscopic sublattice polarization of the A bands is less than that of the B bands, which is allowed due to the lack of any symmetry that interchanges the sublattice.

B. Band-projected interacting model

The continuum model is augmented with long-range dual-gate screened Coulomb interactions $V(q) = \frac{e^2}{2\epsilon_0\epsilon_r q}\tanh qd_{\mathrm{sc}}$, where the relative permittivity $\epsilon_r = 8$ captures the effect of the hexagonal boron-nitride (hBN) dielectric and remote bands, and the screening length $d_{\mathrm{sc}} = 25\,\mathrm{nm}$. A subtraction scheme is required to prevent double-counting interactions, as they already feed into model parameters such as the Fermi velocity [11,21,28,73,74]. We will use the "average" scheme where the electron density is measured with respect to a reference density corresponding to half filling of each flatband at infinite temperature [12,21]. We neglect terms such as intervalley Coulomb and phonon-induced contributions which scatter

electrons between the valleys and are suppressed [75]. The full band-projected Hamiltonian is

$$\mathcal{H} = \frac{1}{2A}\sum_{\boldsymbol{q}\in\mathbb{R}^2} V(\boldsymbol{q})\delta\hat{\rho}_{\boldsymbol{q}}\delta\hat{\rho}_{-\boldsymbol{q}} + \sum_{\boldsymbol{k}\in\mathrm{mBZ}} c^\dagger_{\boldsymbol{k}} h(\boldsymbol{k}) c_{\boldsymbol{k}}, \tag{4}$$

where $A = N_M A_M$ is the total area, $c^\dagger_{\boldsymbol{k}}$ is a moiré band creation operator with spinor structure in flavor and band space, and $\delta\hat{\rho}_{\boldsymbol{q}} = \hat{\rho}_{\boldsymbol{q}} - 4\overline{\rho}_{\boldsymbol{q}}$ is the density measured with respect to half filling of all bands (there are eight bands in total, and we define $\overline{\rho}_{\boldsymbol{q}}$ to be the average band density). We note that while $\boldsymbol{k}$ varies over the mBZ, and labels the states of various Bloch momenta, the momentum $\boldsymbol{q}$ varies over the entire plane because density fluctuations have a continuous profile and vary within a single moiré unit cell.

The forms of the density operators are $\hat{\rho}_{\boldsymbol{q}} = \sum_{\boldsymbol{k}} c^\dagger_{\boldsymbol{k}} \Lambda_{\boldsymbol{q}}(\boldsymbol{k}) c_{\boldsymbol{k}+\boldsymbol{q}}$ and $\overline{\rho}_{\boldsymbol{q}} = \frac{1}{2}(\overline{\rho}^A_{\boldsymbol{q}} + \overline{\rho}^B_{\boldsymbol{q}})$, where $\overline{\rho}^{\tilde{\sigma}}_{\boldsymbol{q}} = \sum_{\boldsymbol{G}} \delta_{\boldsymbol{q},\boldsymbol{G}} \sum_{\boldsymbol{k}} \Lambda^{\tau,\tilde{\sigma}\tilde{\sigma}}_{\boldsymbol{G}}(\boldsymbol{k})$ is the translationally symmetric background density in a periodic gauge $c_{\boldsymbol{k}} = c_{\boldsymbol{k}+\boldsymbol{G}}$. The density operators are written in terms of the form factor matrix $\Lambda^{\tau\tilde{\sigma}\tilde{\sigma}'}_{\boldsymbol{q}}(\boldsymbol{k}) = \langle u^\tau_{\boldsymbol{k}\tilde{\sigma}} | u^\tau_{\boldsymbol{k}+\boldsymbol{q}\tilde{\sigma}'}\rangle$ which consists of the amplitudes for the density operator to scatter Bloch states, $|u^\tau_{\boldsymbol{k}\tilde{\sigma}}\rangle$, at wave vector $\boldsymbol{k}+\boldsymbol{q}$ to $\boldsymbol{k}$. Note that while the form factors depend on τ, the densities do not due to time-reversal symmetry. Since we are in the sublattice basis, $h(\boldsymbol{k})$ is a matrix that is block diagonal in valley and spin but has both diagonal and off-diagonal matrix elements in sublattice $\tilde{\sigma}$.

The interacting Hamiltonian $\mathcal{H}$ has a large set of symmetries [42]. On top of moiré translation and spinless time-reversal symmetry (TRS) $\hat{\mathcal{T}}$, which flips valleys and applies complex conjugation, the system is invariant under threefold rotations $\hat{C}_{3z}$ as well as $\hat{C}_{2y}$, which flips the valley and the top and bottom layers. Note that the action of $\hat{C}_{2z}$ maps $\boldsymbol{\delta} \to -\boldsymbol{\delta}$ and is therefore not a symmetry of $\mathcal{H}$. As we have ignored the small "Pauli" twists in the Dirac terms of Eq. (1) and used the leading harmonic and two-center approximation in the tunneling terms [64], there is a particle-hole-inversion symmetry $\mathcal{IC}$ that also exchanges layers [42]. In flavor space, $\mathcal{H}$ possesses a global $U(2)_K \times U(2)_{\bar{K}}$ symmetry, which includes charge-$U(1)_c$ and valley-$U(1)_v$ conservation as well as independent $SU(2)_s$ spin rotations within each valley.

We will primarily be interested in Hartree-Fock, Slater-determinant states because they arise in strong-coupling perturbation theory and in Hartree-Fock numerics. Such states are characterized by a projector

$$P_{\boldsymbol{k}\tau sn;\boldsymbol{k}'\tau's'n'} = \langle \hat{c}^\dagger_{\boldsymbol{k}\tau sn} \hat{c}_{\boldsymbol{k}'\tau's'n'}\rangle, \quad P = \tfrac{1}{2}(1+Q), \tag{5}$$

where n, n' are band indices either in the BM band basis or the Chern-sublattice basis (in which case we use $\tilde{\sigma}$ instead of n). The filling is determined by $\mathrm{Tr}P = (\nu+4)N_M$, with N_M the number of moiré unit cells. We will also find it convenient to use the matrix Q, which squares to 1 since P is a projector.

In the chiral limit [14], $\kappa = 0$, and at the magic angle, the system has an enhanced symmetry. To see this, we note that at $\kappa = 0$ chiral symmetry enforces that the form factors are diagonal in the sublattice basis and the dispersion $h(\boldsymbol{k})$ vanishes at the magic angle. The Hamiltonian is then just the interaction term, which has $U(2)\times U(2)\times U(2)\times U(2)$ symmetry consisting of independent spin and charge rotations within each sublattice and valley degree of freedom. This limit will be the starting point of the strong-coupling theory in Sec. III.

C. Hartree-Fock calculations

For the HF calculations, we only include fillings $\nu \geqslant 0$ since the physics at negative fillings is related by particle-hole symmetry given our assumptions on H^{BM}. The only other conditions we impose on Eq. (5) are spin collinearity $s = s'$, and restricted TSB. For the latter, the system is allowed to expand its unit cell to double or triple the periods along the moiré axes. To ensure convergence in phase diagrams, each parameter involves >300 initial seeds of different types, and we use the optimal damping algorithm to accelerate convergence [76]. For all plots of the HF band structures, the energies are measured with respect to the Fermi level.

III. STRONG-COUPLING STATES AT INTEGER FILLINGS

In this section we report on a strong-coupling approach [13] to h-HTG, where the noninteracting dispersion and chiral symmetry breaking are taken as perturbations. Detailed calculations are provided in Appendix A of Ref. [77]; here we summarize the structure of the results, the physical intuition behind them, and their implications.

Strong-coupling states, or generalized quantum Hall ferromagnets, Pauli block the density mediated scattering between Bloch states so that the only contribution of the interaction term comes from the overall charging energy associated with reciprocal lattice wave vectors $\boldsymbol{G}$. Let us briefly review this argument. Consider states $|\Psi_0\rangle$ that fully fill some combination of sublattice and valley polarized bands, characterized by Hartree-Fock projectors $P = \frac{1}{2}(1+Q)$ that are diagonal in sublattice and valley and $\boldsymbol{k}$ independent; here Q is an 8×8 matrix with eigenvalues ± 1 that correspond to filled and empty bands respectively. We do not enforce that the state is diagonal in spin, as the entire sphere of spin directions is degenerate for each sublattice and valley under the enhanced symmetry. Then, the density operator at wave vector $\boldsymbol{q} \neq \boldsymbol{G}$ cannot scatter within a flavor due to Pauli blocking, and cannot scatter between flavors because the form factor is diagonal in this basis. We therefore conclude that $|\Psi_0\rangle$ is annihilated by $\rho_{\boldsymbol{q}\neq\boldsymbol{G}}$. The strong-coupling states are eigenvectors of the density operator at reciprocal lattice wave vector $\boldsymbol{G}$, and therefore eigenvectors of the interaction Hamiltonian. The associated eigenvalue of the interaction Hamiltonian can be interpreted as a classical "Hartree" charging energy that measures how well the charge density of the state $|\Psi_0\rangle$ cancels against the background charge $-4\overline{\rho}_{\boldsymbol{G}}$.

The Hartree charging energy yields a splitting of the unperturbed strong-coupling states that depends on both the filling relative to charge neutrality, $\nu = \frac{1}{2}\mathrm{tr}\, Q$, and the sublattice polarization $\nu_z = \frac{1}{2}\mathrm{tr}\, Q\sigma_z$. Explicitly, we have

$$\frac{E_H}{N_M} = \nu^2\Omega_{00} + 2\nu\nu_z\Omega_{0z} + \nu_z^2\Omega_{zz}, \tag{6}$$

where

$$\Omega_{00} = \frac{1}{2A_M}\sum_{\boldsymbol{G}} V_{\boldsymbol{G}}\overline{\rho}_{\boldsymbol{G}}\overline{\rho}_{-\boldsymbol{G}},$$
$$\Omega_{0z} = \frac{1}{2A_M}\sum_{\boldsymbol{G}} V_{\boldsymbol{G}}\overline{\rho}_{\boldsymbol{G}}\overline{\rho}^{z}_{-\boldsymbol{G}},$$
$$\Omega_{zz} = \frac{1}{2A_M}\sum_{\boldsymbol{G}} V_{\boldsymbol{G}}\overline{\rho}^{z}_{\boldsymbol{G}}\overline{\rho}^{z}_{-\boldsymbol{G}}. \tag{7}$$

Here $\overline{\rho}^{z}_{\boldsymbol{G}} = \sum_{\boldsymbol{k}} \Lambda^{\tau z}_{\boldsymbol{G}}(\boldsymbol{k}) = \frac{1}{2}(\rho^{A}_{\boldsymbol{G}} - \rho^{B}_{\boldsymbol{G}})$ is the difference in density between sublattices, which does not depend on valley τ due to time-reversal symmetry, and $\Lambda^{\tau z}_{\boldsymbol{G}}(\boldsymbol{k}) = \frac{1}{2}[\Lambda^{\tau A}_{\boldsymbol{G}}(\boldsymbol{k}) - \Lambda^{\tau B}_{\boldsymbol{G}}(\boldsymbol{k})]$. At charge neutrality, states with $\nu = \nu_z = 0$ are exact zero modes of the interaction Hamiltonian, since here the background density is perfectly canceled. Note that in practice $\Omega_{0z} \approx 0.02$ meV and $\Omega_{zz} \approx 0.003$ meV such that the splitting between states with different ν_z is small.

The appearance of sublattice polarization in the strong-coupling Hartree energetics is in contrast to TBG, where the charging energy only depends on filling due to an approximate particle-hole symmetry that relates the density of the two sublattices at the same position $\boldsymbol{r}$. Furthermore, strong-coupling intervalley-coherent (IVC) states are competitive in TBG [11,12]: both valleys of TBG have bands with $C = \pm 1$, and each Chern sector has an approximate $U(4)$ symmetry that rotates not only spin but also valley, thereby relating valley polarized and IVC states [11,78,79]. There can be no such symmetry in h-HTG; in fact, all four Chern numbers of the sublattice-valley bands are distinct such that off-diagonal orders must have vortices in the mBZ, equal in number to the difference in Chern number, where the order parameter vanishes [39].

The strong-coupling states are further split upon including both the chiral symmetry-breaking, sublattice off-diagonal, part of the form factor, $\Lambda^{o}_{\boldsymbol{q}}(\boldsymbol{k}) = \frac{1}{2}[\Lambda - \tilde{\sigma}_z \Lambda^{o}_{\boldsymbol{q}}(\boldsymbol{k})\tilde{\sigma}_z]$, which is nonzero for $\kappa > 0$, as well as the dispersion $h(\boldsymbol{k})$. The chiral symmetry breaking form factor leads to exchange energy penalties for states that do not completely fill a spin-valley flavor. Indeed, within a single spin and valley, if only the A sublattice is filled, say, then the form factor can scatter A electrons to sublattice B and back, leading to an exchange penalty. This effect, which contributes to first order in perturbation theory, favors the spin and valley flavors to be fully filled or fully empty such that this exchange is Pauli blocked. Another way to characterize this is "ferromagnetism between sublattices" induced by exchange: (de)occupation of the A sublattice within a flavor favors (de)occupation of the B sublattice within the same flavor. In contrast, the dispersion $h(\boldsymbol{k})$ has a part that tunnels electrons between the two sublattices which vanishes in first order in perturbation theory, but at second order favors "antiferromagnetism between sublattices" through "superexchange," similar in spirit to the antiferromagnetic exchange between spins induced by hopping in the Hubbard model. In total, we obtain the splitting per moiré unit cell

$$\frac{E_{\text{split}}}{N_M} = \frac{1}{4}(J-\lambda)\text{tr}\,(Q\sigma_x)^2 = \frac{1}{2}(J-\lambda)\text{tr}\,Q_A Q_B, \tag{8}$$

where $Q_{A,B}$ are the 4×4 blocks of Q corresponding to the A and B sublattice respectively, $J \sim h_o^2/U$ is the superexchange scale induced by the off-diagonal dispersion, and $\lambda \sim |\Lambda^o|^2$ is the exchange penalty associated with the off-diagonal form factor. Figure 3 illustrates these mechanisms for example states at charge neutrality. The derivation of Eq. (8) is given in Appendix A of Ref. [77]. Note that the (super)exchange scales $J, \lambda \gtrsim 1$ meV are significantly larger than the ν_z-splitting scales Ω_{0z}, Ω_{zz}, but smaller than the interaction scale $\approx$30 meV.

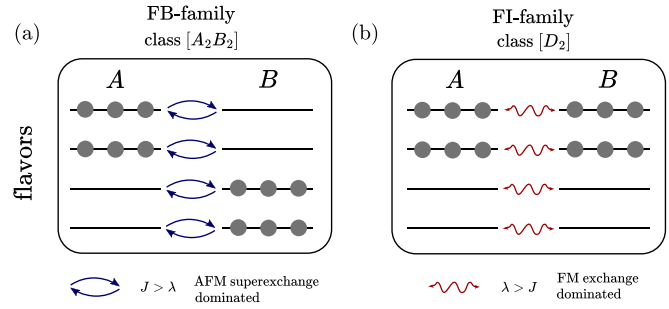

FIG. 3. Strong-coupling sublattice superexchange and exchange. (a) An example of a strong-coupling state at $\nu = 0$ in the flavor-balanced (FB) family that maximally benefits from the dispersion-induced superexchange J. (b) An example in the flavor-imbalanced (FI) family that maximally benefits from the exchange λ that arises due to a finite chiral ratio. Note that we do not explicitly label the spin-valley flavors to reflect the "flavor permutation symmetry" for Slater determinants [see the discussion around Eq. (9)].

A. Hierarchical labeling of strong-coupling phases

We outline a compact notation for describing strong-coupling insulators at integer fillings ν, which is indispensable given the multiple symmetries of $\mathcal{H}$. A strong-coupling insulator $|\psi\rangle$ is one that can be obtained via small deformations of a reference state $|\phi\rangle$ consisting of $\nu + 4$ fully occupied Chern bands. By "smooth deformations," we mean that $|\psi\rangle$ and $|\phi\rangle$ share the same symmetries, have comparable Chern band occupations $\langle n_{\tau s\tilde{\sigma}}\rangle$ (where $n_{\tau s\tilde{\sigma}} = \sum_k d^{\dagger}_{k\tau s\tilde{\sigma}} d_{k\tau\tilde{\sigma}}$), and can be connected without closing the gap. Hence the Chern number is determined simply by summing the corresponding $C_{\tau s\tilde{\sigma}}$ of the filled Chern bands [Eq. (3)]. Based on the arguments of the previous section, we expect that such strong-coupling states are the ground state, at least sufficiently close to the chiral limit at the magic angle.

Moving forward we will make the assumption that spin in the z direction is conserved, i.e., $[Q, S_z] = 0$ such that Q is diagonal in spin. While generic strong-coupling states need not satisfy this, we argue in Appendix B of Ref. [77] that all ground states are symmetry related to a state with conserved S_z. We can then label strong-coupling ground states with the sublattice filling for each S^z spin and valley. The projector is then $P = \text{diag}(N^{\tau s}_{\tilde{\sigma}})$, an 8×8 diagonal matrix with $N^{\tau s}_{\tilde{\sigma}} = 0, 1$ labeling whether the band is filled or empty. We will use $\alpha = (\tau, s)$ as a combined index for both spin and valley, so that $\nu - 4 = \sum_{\alpha\tilde{\sigma}} N^{\tau s}_{\tilde{\sigma}}$, and $\nu_z = \sum_{\alpha\tilde{\sigma}} \tilde{\sigma} N^{\tau s}_{\tilde{\sigma}}$.

The separation of energy scales indicated by the strong-coupling analysis suggests a natural hierarchical labeling scheme of strong-coupling states, summarized by Fig. 4.

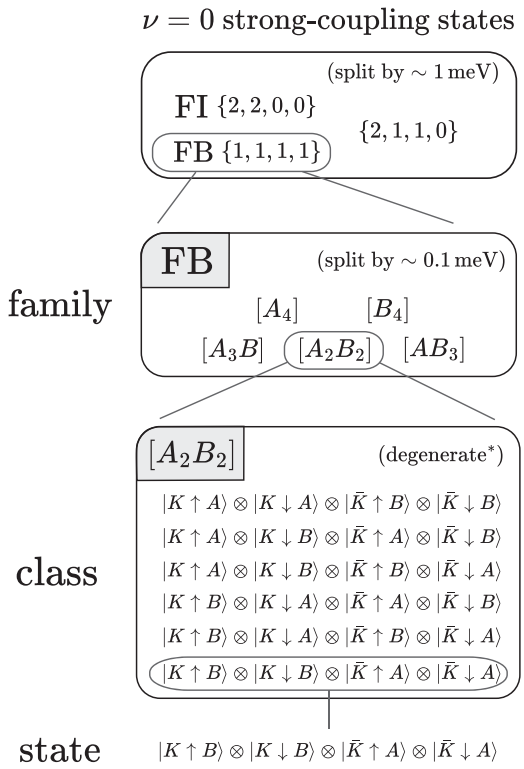

FIG. 4. Hierarchy of strong-coupling states at $\nu = 0$. The figure illustrates how the particular state $|\psi\rangle = |K\uparrow A\rangle \otimes |K\downarrow A\rangle \otimes |\bar{K}\uparrow B\rangle \otimes |\bar{K}\downarrow B\rangle$ fits into the broader energetic hierarchy of strong-coupling states. Starting from the bottom of the figure, $|\psi\rangle$ is part of the $[A_2B_2]$ class whose states share the same occupations modulo relabeling of spin-valley labels (i.e., two flavors with an occupied A band and two flavors with an occupied B band), and are degenerate within mean-field theory for our Hamiltonian [Eq. (4)]. Different classes are split depending on the sublattice polarization [Eq. (6)]. $[A_2B_2]$ in turn is part of the flavor-balanced (FB) family at $\nu = 0$ which has equal occupation $\{1, 1, 1, 1\}$ of all flavors. FB and two other families [split by the differing flavor occupations according to Eq. (8)] together comprise the manifold of $\nu = 0$ strong-coupling states.

The most significant splitting is due to the sublattice exchange-superexchange term [Eq. (8)], which separates states into "families" separated by energies of order $\approx$1 meV. For $J < \lambda$, the term $\mathrm{tr}\, Q_A Q_B = \sum_\alpha (N_A^\alpha - \frac{1}{2})(N_B^\alpha - \frac{1}{2})$ in Eq. (8) favors as many double and empty occupations, $N_A^\alpha = N_B^\alpha$, as possible, while for $J > \lambda$ it is best for flavors to be as singly occupied as possible (see Fig. 3). This term dictates the overall distribution among the flavors, agnostic to the details of the specific spin/valley/sublattice bands being filled. We therefore label each family by the flavor occupation numbers $\{N_{f_0}, N_{f_1}, N_{f_2}, N_{f_3}\}$, where $N_{f_i} \in 0, 1, 2$ are listed in descending order. Different families are distinguished based on the number of fully filled, singly occupied, and empty flavors.

As discussed above, the family that doubly occupies as many flavors as possible is favored for $\lambda > J$; we will call this family "maximally flavor imbalanced" (FI). Meanwhile, the family that has as few doubly occupied flavors as possible is called "maximally flavor balanced" (FB), and is favored for $J > \lambda$. For $\nu = 0$, the FI and FB family correspond to the $\{2, 2, 0, 0\}$ and $\{1, 1, 1, 1\}$ labels (illustrated in Fig. 3). Note that $\nu = 3$ only has one family, $\{2, 2, 2, 1\}$, which we arbitrarily designate as FB. The description in terms of flavor occupations is also useful beyond the strong-coupling regime, and can be applied to TSB phases and noninteger fillings.

The states within a given family are further separated into distinct "classes" based on their overall sublattice polarization ν_z [Eq. (6)], which are separated by smaller energies of order $\approx$0.1 meV. A descriptive labeling of a particular class is achieved by the notation $[D_{N_D} A_{N_A} B_{N_B}]$, where N_A (N_B) counts the flavors where only the A (B) band is filled, and N_D counts the fully filled flavors where both A and B are occupied. These integers satisfy $N_A + N_B + 2N_D = \nu + 4$. We consider some examples: For $\nu = 3$, the class $[D_3 A_0 B_1]$ (or, $[D_3 B]$ for short) refers to any state where all bands are filled except for one of the A bands: $(K\uparrow A)$, $(K\downarrow A)$, $(\bar{K}\uparrow A)$, or $(\bar{K}\downarrow A)$. At charge neutrality $\nu = 0$, the class $[A_2B_2]$ means two flavors have only the A band occupied, and the other two flavors have only the B band occupied. Note that the valley degree of freedom allows for multiple possible Chern numbers—the class $[A_2B_2]$ includes states with $C = -6, 0, 6$.

The states within a class are exactly degenerate within our strong-coupling analysis and self-consistent HF theory. This can be understood due to the presence of a "flavor permutation symmetry" that exists for Slater determinant states of h-HTG that are S^z and valley conserving. For instance, the strong-coupling energetics outlined in the previous paragraph are invariant under permutations of the $\alpha = (\tau, s)$ index. This is a consequence of the fact that the Fock energy decomposes into a sum over contributions from each flavor:

$$E_F[P] = \sum_\alpha E_{F\alpha}[P_\alpha], \tag{9}$$

where $E_{F\alpha}$ for different α are symmetry related, while the Hartree energy depends only on the total density (see Appendix C of Ref. [77]). This flavor permutation symmetry can result in very physically distinct states having equivalent HF energies. For example, consider a quantum spin Hall insulator at $\nu = +2$, consisting of filling all Chern-sublattice bands except for $(K\uparrow A)$ and $(\bar{K}\downarrow A)$. By exchanging the flavors $(\bar{K}, \downarrow) \leftrightarrow (K, \downarrow)$, through TRS applied on spin $\downarrow$, we arrive at a valley polarized $|C| = 2$ Chern insulator.

The application of time reversal to only one spin species only makes sense at mean-field level as a result of the decoupling Eq. (9); this "Hartree-Fock symmetry" does not make sense either as a unitary or antiunitary symmetry on the full Hilbert space, and the degeneracy between the CI and QSH is expected to be lifted by quantum fluctuations outside of mean-field theory. From the strong-coupling perspective, they could be split in sufficiently high-order perturbation theory in the dispersion $h(\boldsymbol{k}) \neq 0$; in the leading-order calculation of J described in the previous subsection, the perturbed state is still a Slater determinant (see Appendix A of Ref. [77]). We note that while some of the flavor permutation induced degeneracies can be lifted by including terms like the intervalley-Hund term, which reduces $SU(2)_K \times SU(2)_{\bar{K}} \to SU(2)_s$, the degeneracy between the QSH and CI only depends on time reversal and requires going beyond mean-field theory. There is another mechanism that is expected to favor the QSH when considering the three-dimensional nature of real space, which is that

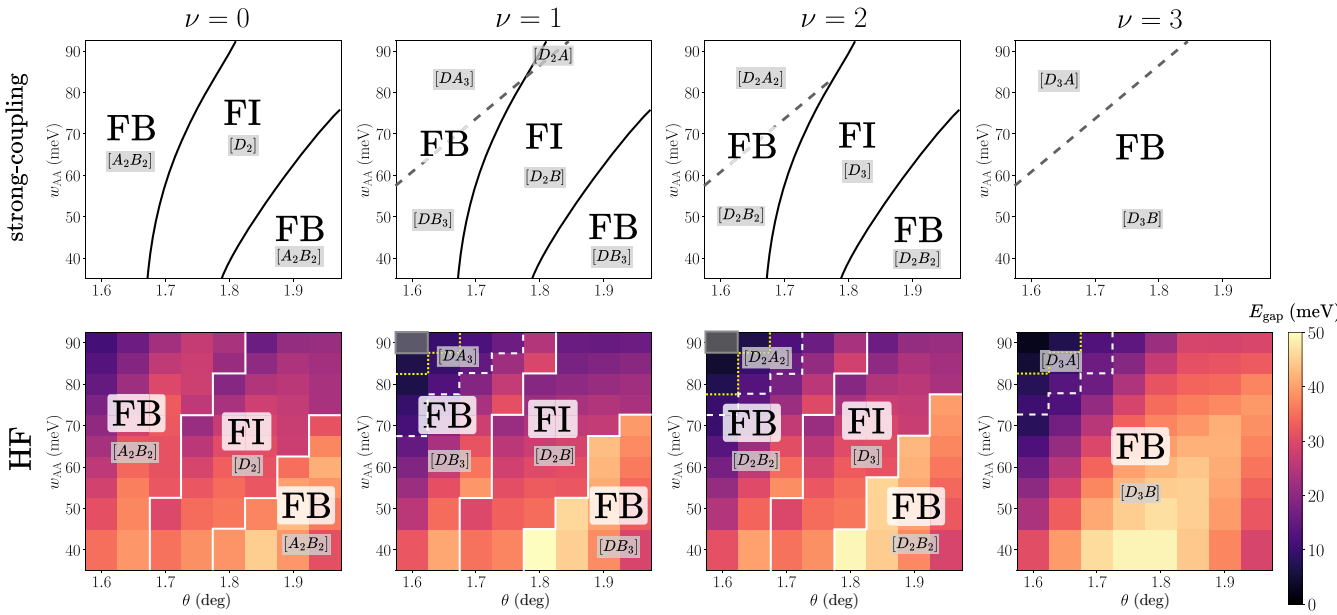

FIG. 5. Phase diagrams for non-negative integer fillings ν at zero displacement field. w_{AA} denotes same-sublattice interlayer tunneling (w_{AB} is fixed at 110 meV). FB and FI, which stand for maximally flavor-balanced and maximally flavor-imbalanced respectively, represent different families of nearly degenerate strong-coupling phases that are distinguished by the patterns of flavor occupations (see Table I). Bracketed labels $[D_{N_D}A_{N_A}B_{N_B}]$ with gray background denote the precise strong-coupling class with minimal energy. N_D, N_A, N_B refer to the number of flavors that are fully filled, have only the A band filled, or have only the B band filled, respectively. Top: Phase diagrams derived from strong-coupling analysis. Black solid lines separate regions that favor the FB (FI) family due to $J > \lambda$ ($J < \lambda$) [see Eq. (8)]. For $\nu > 0$, gray dashed lines separate regions that favor polarization into the A (B) sublattice due to $\Omega_{0z} < 0$ ($\Omega_{0z} > 0$) [see Eq. (6)]. Bottom: Numerical self-consistent Hartree-Fock (HF) phase diagrams. Color plot shows the HF band gap E_{gap}. White solid lines indicate dominant boundaries, shaded gray areas denote absence of a charge gap, and dotted yellow lines indicate a weak-coupling excitonic instability. Dashed white lines indicate transitions between strong-coupling classes within the same family. System size is 12×12, and relative permittivity $\epsilon_r = 8$.

the CI generally has a finite orbital magnetization and hence a magnetic field energy cost. Although these magnetic fields vanish in an infinite 2D system, recall that h-HTG appears only as a finite domain of the full HTG supermoiré structure, and so such effects may be non-negligible. We leave a detailed analysis of such effects for future work.

The possible combinations of sublattice polarizations and flavor permutations lead to a multitude of states with varying topological numbers and associated quantized charge, spin, and valley Hall responses. The total Chern number C of any strong-coupling state can be straightforwardly obtained using Eq. (3), since the total Chern number of all remote bands vanishes (the two valleys cancel each other due to TRS). However, the valley Chern number C_v is more subtle as the remote bands have a nontrivial contribution, which is explained in detail in Appendix D of Ref. [77].

B. Strong-coupling phase diagram

In the top row of Fig. 5, we show the strong-coupling prediction for the phase diagrams as a function of w_{AA} and θ. The main phase boundaries (solid lines) reflect the competition between the different families FB and FI, which is controlled by the relative values of J and λ [Eq. (8)]. Within each family, there are also secondary phase boundaries (dashed lines) separating distinct classes, based on the sublattice polarization ν_z if some flavors are partially occupied [Eq. (6)]. At charge neutrality $\nu = 0$, we always have $\nu_z = 0$ since Ω_{zz} is positive. At finite integer fillings, the favored sublattice is set by the sign of Ω_{0z} (since, for our range of parameters, Ω_{zz} is usually very small); while Ω_{0z} is positive (favoring the B sublattice) for much of the phase diagram considered, we find it becomes negative at small twist angles and large w_{AA}. These findings are in excellent agreement with the self-consistent HF calculations discussed in the next section.

IV. HARTREE-FOCK PHASE DIAGRAM AT INTEGER FILLINGS

The bottom row of Fig. 5 shows the integer HF phase diagrams as a function of w_{AA} and twist angle θ. Almost all regions show a nonzero HF gap E_{gap}, indicating the presence of correlated insulators for the chosen parameters. As expected from the narrow BM dispersion and strong interactions, the insulators are all strong-coupling phases (see Sec. III A), as confirmed by the substantial polarization in flavor and Chern-sublattice space. The positions of the phase boundaries (white solid and dashed lines) are remarkably similar across all fillings. For $\nu = 0, 1, 2$, the phase diagrams are dominated by two different strong-coupling classes, whose sublattice-flavor occupations are indicated with a gray background. One of them is the ground state for a window of twist angles near the magic angle $\theta = 1.8^\circ$, while the other emerges for slight

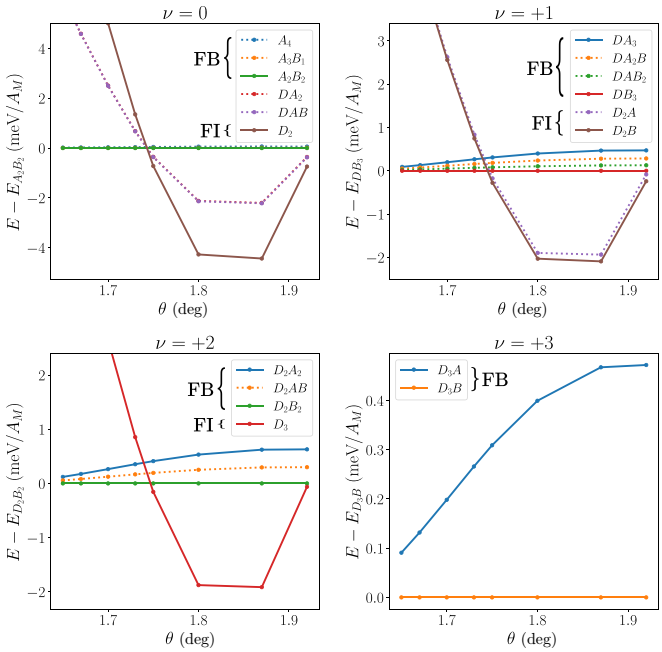

FIG. 6. Energetic competition between strong-coupling phases at zero displacement field. Self-consistent HF energies of different strong-coupling classes. They are labeled according to the configuration of occupied sublattice bands, e.g., DB_3 indicates one fully filled flavor and three additional filled B bands in singly occupied flavors. Phases that appear in Fig. 5 are denoted with solid lines. States with the same number of fully occupied flavors belong to the same family (see Table I) and are nearly degenerate. For $\nu = 0$, we have omitted classes which are related by particle-hole symmetry to the ones shown (e.g., $E_{DA_2} = E_{DB_2}$). Note that no energies in the figures are degenerate with each other, though the splittings at $\nu = 0$ are almost invisible on this scale. System size is 12×12, $w_{AA} = 70$ meV.

detuning away from this. For $\nu = 1, 2, 3$, another strong-coupling class appears in the top-left corner.

For each parameter, our HF calculations produce a particular strong-coupling class $[D_{N_D}A_{N_A}B_{N_B}]$ with the lowest energy. However, Fig. 6 shows that the energies of multiple strong-coupling classes can be closely competitive. Recall that even within a class, there are multiple distinct patterns of symmetry-breaking and Chern numbers. At each filling, the classes group into families depending on the number of fully occupied flavors N_D, which determines the energetics under exchange λ and superexchange J, as described by Eq. (8). The family with the maximum possible $N_D = \lfloor \frac{\nu+4}{2} \rfloor$ is denoted FI (maximally flavor imbalanced), and is favored near the magic angle where the noninteracting bandwidth is smallest such that exchange outweighs superexchange $\lambda > J$. In contrast, the family with the minimum possible N_D, denoted FB (maximally flavor balanced), is favored for larger bandwidths where superexchange between sublattices outweighs exchange. For $\nu = 0$, there is also an intermediate family with $N_D = 1$, which we do not name since it does not appear as the ground state in Fig. 5. The possibilities are summarized in Table I. These families are separated by energies $\gtrsim$1 meV except near the phase boundaries. The dependence of the FB vs FI competition on chiral ratio and twist angle matches closely with the perturbative strong-coupling analysis. However, consistent

TABLE I. Families of strong-coupling states. At a fixed filling, each family includes different classes distinguished by the sublattice occupations (see main text). {flavor occ.} lists the flavor occupations in descending order. The FB (FI) family minimizes (maximizes) the number of fully filled flavors. C denotes the possible Chern numbers, with large bold entries corresponding to the dominant ground-state HF phases obtained in Fig. 5.

Family	ν	{flavor occ.}	$\lvert C\rvert$
FB	0	{1, 1, 1, 1}	**0**, **6**, 3
	1	{2, 1, 1, 1}	**1**, 2, 4, 5
	2	{2, 2, 1, 1}	**0**, **2**, 1, 3, 4
	3	{2, 2, 2, 1}	**1**, 2
FI	0	{2, 2, 0, 0}	**0**, **2**
	1	{2, 2, 1, 0}	**0**, **2**, 1, 3
	2	{2, 2, 2, 0}	**1**
	0	{2, 1, 1, 0}	0, 1, 2, 4

with the strong-coupling analysis of Eq. (6), the splittings within each family from distinct ν_z are significantly smaller, especially at $\nu = 0$ where the differences are $\lesssim 0.05$ meV. These sensitive near degeneracies can easily be affected by details of the modeling, as well as extrinsic effects such as sublattice coupling to the hBN substrate. Therefore, while our prediction of the lowest-energy strong-coupling family is robust and in excellent agreement with strong-coupling perturbation theory in Sec. III, the particular strong-coupling class and state that ultimately emerge may be sensitively detail dependent. To reflect this, the phase diagrams of Fig. 5 also label the relevant strong-coupling family. At $\nu = +3$, there is only a single option for the family since we must have $N_D = 3$. In Table I, we also list the possible Chern numbers, with the bold entries corresponding to the lowest-energy representatives over major parts of the phase diagrams.

The emergence of symmetry-broken Chern insulators should give rise to several characteristic features in experimental observables. In devices consisting of a single h-HTG region spanning the electrical contacts, these states spontaneously break TRS and will exhibit a quantized anomalous Hall response. More likely, however, experimental detection of such signatures in transport will be complicated by the supermoiré structure of HTG which consists of h-HTG domains and their $\hat{C}_{2z}$-related $\bar{\text{h}}$-HTG counterparts [42]; we defer a detailed discussion to Sec. VI. The Chern insulators can also be uncovered by applying a perpendicular magnetic field and studying the ν-B plane, where such states appear as sloped lines according to the Streda formula. This method allows for the identification of multiple competing states which are rooted at the same integer filling but have different Chern numbers C (Table I), and is also accessible to probes such as scanning tunneling microscopy (STM) [26,34,52,80–84] and scanning electron transmission (SET) [38,85,86] which can map out the local moiré-scale physics.

In many magic-angle graphene systems, the real-space charge inhomogeneity of a filled central band within the moiré cell leads to substantial interaction-induced renormalization, especially at finite fillings. For instance, the total charge density of the flatbands in TBG is strongly concentrated at AA-stacking regions, though the Bloch wave functions at different

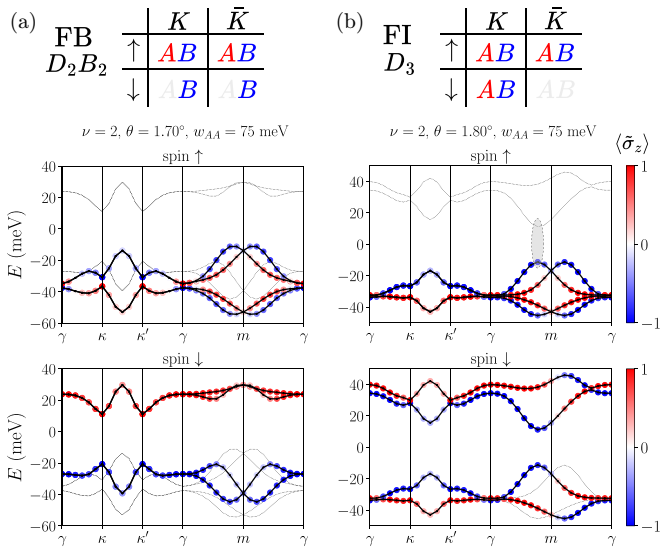

FIG. 7. Strong-coupling phases at $\nu = +2$. (a) Top shows the occupations in the sublattice-polarized basis for a low-Chern $C = 0$ representative of D_2B_2 phase (FB family). Bottom shows the HF band structures in each spin sector, with colored dots indicating the Chern basis polarization. The opposite spin bands are also shown with thin dotted lines. (b) Same as (a) but for a $C = -1$ representative of the D_3 phase (FI family). Shaded oval indicates an incipient intervalley excitonic instability. System size is 18×18.

mBZ momenta have different spatial localization properties. In particular, the Bloch function at γ is more diffusely spread around the AA regions compared to other momenta. Hence, at positive fillings, the Hartree-renormalized dispersion experiences a pronounced dip at γ, substantially increasing the bandwidth from its noninteracting value [15–21]. This complicates the identification of the correct starting point for theoretical treatments of various phenomena. In h-HTG, the presence of two shifted moiré patterns (Fig. 1) means that the flatband charge density is distributed across two AA peaks, rather than concentrated around a single point as is the case in TBG. As a result, the Hartree-induced warping of the bands should be less severe. This expectation is borne out in Fig. 7, which plots the self-consistent HF band structure for the $[D_2B_2]$ and $[D_3]$ phases at $\nu = +2$. The bands are color coded by the Chern basis polarization, which reveals the strong-coupling nature of the states. By comparing with the dispersion and sublattice polarization of the noninteracting bands (Fig. 2), it is clear that the bands are not significantly deformed, in contrast to other moiré systems. For instance, the pronounced dispersion of the B bands along the γ-m lines is preserved.

This "band rigidity" is also conducive towards the stabilization of insulators at nonzero fillings. In TBG, the Hartree corrections progressively degrade the mean-field exchange gap at large fillings, such that the strong-coupling candidates at $|\nu| = 3$ have a vanishing/small gap which is sensitive to details of the modeling, and may give way to other candidate states [12,28,87–89]. On the other hand, the HF gap in h-HTG remains similar across all integer fillings (Fig. 5), suggesting that the insulating character will be more robust against quantum fluctuations and other deleterious effects like disorder. Note that the FB family has a larger insulating gap than the FI family for $|\nu| > 0$, since all of the dispersive B bands are either above or below the Fermi level.

To see the interaction renormalization more explicitly, we plot the Hartree and Fock components of the mean-field Hamiltonian corresponding to the fully filled $\nu = +4$ symmetry-preserving state in Fig. 8(a). The potentials are shown for the diagonal entries in the Chern-sublattice basis, and we normalize E_{Hartree} by $1/4$ to estimate the contribution from a single filled band. As in TBG, the direct and exchange terms tend to cancel each other somewhat. However, the Hartree part is significantly suppressed compared to TBG. Figure 8(b) illustrates the HF band structure for a strong-coupling insulator at $\nu = +3$ where the nearest remote bands have also been included self-consistently. Note that the energy axis has not been zeroed to the chemical potential, and we have subtracted off a classical charging energy arising from $V(0)$. Even though the system is far from neutrality and develops an appreciable exchange splitting, there remains a sizable gap to the remote bands, whose position and shape are qualitatively unchanged. There is negligible remote band mixing, as the central bands retain $\gtrsim$99.5% fidelity. This is enabled by the large initial remote gap in the noninteracting dispersion, and the absence of strong momentum-dependent Hartree corrections. Therefore, unlike in many other strongly interacting moiré systems, we anticipate the approximation of restricting to the central bands for interacting calculations to remain quantitatively correct all the way to $|\nu| = 4$. The suppression of Hartree should also lead to a smaller overall positive offset to the filling-dependent inverse electronic compressibility $d\mu/dn$.

It has been proposed that the combination of ideal quantum geometry and suppressed interaction renormalization in h-HTG is potentially conducive towards realizing fractional Chern insulators, especially at fractional fillings beyond $|\nu| = 3$ [42]. Figure 9(a) shows that for most of the phase diagram at $\nu = +3$, the lowest-energy strong-coupling phase is $[D_3B]$, which has a single narrow conduction band in the less dispersive A sublattice with $|C| = 1$. In Fig. 9(b), we chart the conduction bandwidth W_{cond}, demonstrating that it remains small $W_{\text{cond}} \lesssim 15$ meV over most of the phase diagram. Furthermore, the fact that the conduction band is nearly wholly composed of one sublattice band suggests that it retains its favorable quantum geometry.

We caution that the energetically preferred flavor and sublattice polarization at integer fillings may not necessarily reflect the situation at finite doping. For instance, while the mean-field ground state at $\nu = 3$ is $[D_3B]$ (we use the terms "state" and "class" interchangeably here), Fig. 6 shows that the $[D_3A]$ state differs in energy by less than 1 meV per moiré cell. Simple considerations of the contrasting dispersion of A and B bands suggest that beyond some finite electron doping the system may experience a first-order transition where the Chern-sublattice polarization switches sign. This is because electron doping a $[D_3A]$ state involves adding carriers to the unoccupied B band, which contains more significant energy troughs compared to the A band [Fig. 2(a)]. Hence doped electrons are less costly if the parent insulator is $[D_3A]$ rather than $[D_3B]$. It is possible then that at some critical filling $3 + \delta_c$, this discrepancy is enough to overcome the initial

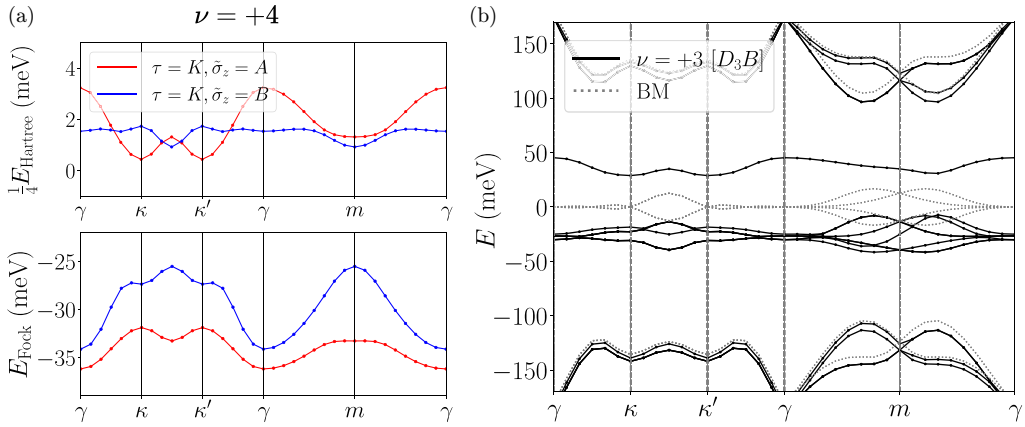

FIG. 8. Hartree-Fock potentials and remote bands. (a) Hartree (divided by 4) and Fock potentials corresponding to the fully filled state at $\nu = +4$. We show the diagonal component in the Chern-sublattice basis and for valley K. (b) Black lines show HF band structure for a state in the $\nu = +3$ $[D_3B]$ strong-coupling class [see Fig. 9(a) for schematic] when including the lowest remote bands self-consistently. Energies are not measured relative to the chemical potential. Dotted gray lines show the noninteracting BM bands. System size is 18×18, $\theta = 1.80°$, $w_{AA} = 75$ meV, and $\epsilon_r = 8$ for interacting calculations.

energy difference of the parent insulators. The precise value of δ_c, if this mechanism does indeed occur, is sensitive to details such as the initial energy splitting between $[D_3A]$ and $[D_3B]$ and the correlation energy of the partially filled band. Similar considerations apply between other integer fillings, and may factor into potential "reset" and cascade physics [80,90]. In TBG, such effects are often explained with flavor transitions, but here the additional possibility of first-order sublattice transitions complicates the picture.

Finally, we discuss the impact of tuning the interaction strength. In Fig. 10, we plot the phase diagram at even integer fillings as a function of ϵ_r and θ. Consistent with the FI family favoring a narrower bandwidth (since dispersion increases J), the twist angle window where FI has the lowest energy shrinks in favor of the FB family when weakening interactions (increasing ϵ_r). We also note that when the band gap is sufficiently small, the strong-coupling phases can be susceptible to a weak-coupling excitonic instability, indicated by yellow dotted lines in Figs. 5 and 10. The relevant exciton is composed of electrons and holes at the B band extrema—an example is highlighted in Fig. 7(b). Depending on the flavor nature of the exciton, this can occur in the intervalley channel and break $U(1)_v$, possibly with a finite (incommensurate) moiré wave vector. However, the change in Chern basis occupations is minor, and the resulting state retains most properties of the nonexcitonic parent phase. Hence, such effects will be difficult to detect experimentally. For sufficiently weak interactions at nonzero ν, the strong-coupling phases can be replaced by gapped TSB phases such as a commensurate Kekulé spiral (KS_κ) or CDW, which will be elaborated on later in the context of finite displacement fields (Sec. V). Sizable regions of the phase diagram can also become gapless, especially for smaller twist angles where the interaction is relatively weaker for fixed ϵ_r due to the increased moiré length.

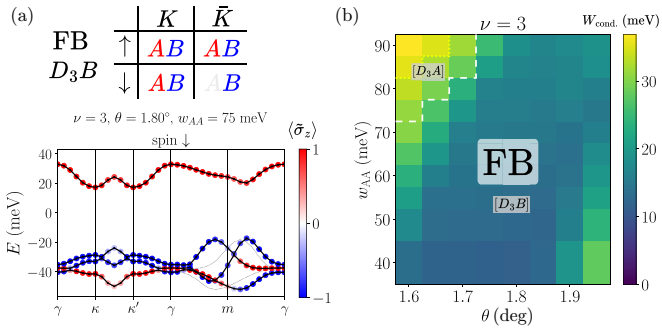

FIG. 9. Strong-coupling Chern insulator at $\nu = +3$. (a) Top shows the occupations in the sublattice-polarized basis for the $C = 1$ state in the D_3B class. Bottom shows the HF band structures in the partially occupied spin sector, with colored dots indicating the Chern-sublattice polarization. The opposite spin bands are also shown with thin dotted lines. System size is 18×18. (b) HF conduction bandwidth W_{cond} as a function of w_{AA} and θ. System parameters identical to those of Fig. 5.

V. FINITE DISPLACEMENT FIELD

Figure 11 illustrates the evolution of the noninteracting band structure as a function of the interlayer potential U. The overall bandwidth widens as U increases, but the most

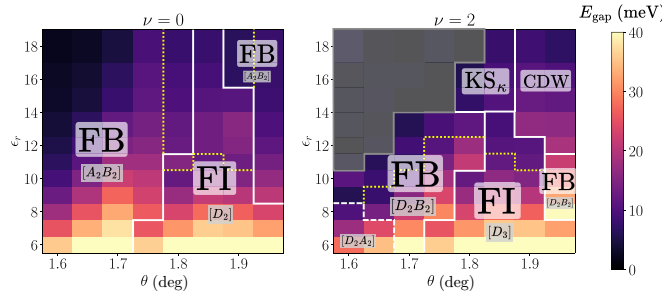

FIG. 10. Effect of tuning interaction strength at zero displacement field. Color plot shows the Hartree-Fock band gap E_{gap}. Labeling is the same as Fig. 5. System size is 12×12 and $w_{AA} = 75$ meV. CDW, charge density wave; KS_κ, Kekulé spiral.

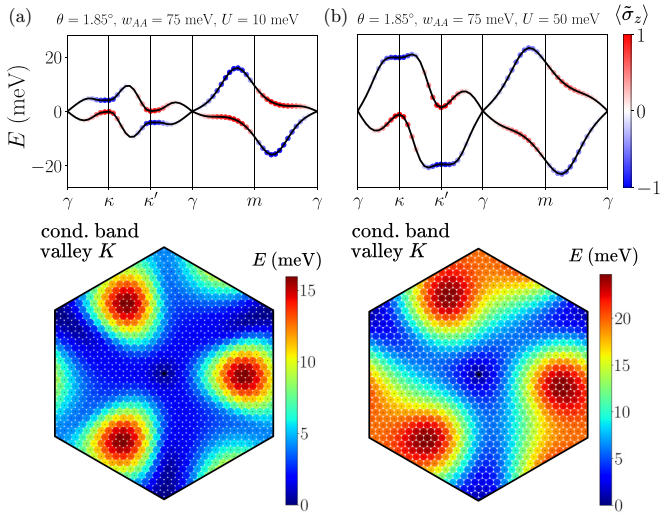

FIG. 11. Noninteracting band structure at finite displacement field. (a) Top shows dispersion of the central bands with interlayer potential $U = 10\,\text{meV}$. Only valley K is shown. Color indicates Chern-sublattice polarization $\langle\tilde{\sigma}_z\rangle$. Bottom shows energy dispersion of the conduction band in the mBZ. (b) Same as (a) except with $U = 50\,\text{meV}$.

significant changes occur at the mBZ corners. At zero displacement field, the bands are nearly degenerate at $E = 0$ around the moiré minivalleys [Fig. 2(a)], but split into sublattice polarized bands for finite U. While the A sublattice remains close to $E = 0$, the B sublattice shifts significantly in energy with opposite signs at κ and κ'. This is because the B bands carry a significant momentum-dependent layer dipole moment. The color plots in Fig. 11 show that the previously isolated high-energy lobes in the mBZ merge into a single "fidget-spinner" feature centered around κ (κ') in valley K ($\bar{K}$) for large U.

The HF phase diagrams as a function of interlayer potential and twist angle are presented in Fig. 12, which show mostly gapped states. At $U = 0$, we recover the strong-coupling phases discussed in Sec. IV. As demonstrated in Fig. 13, the delicate competition between strong-coupling classes in the same family persists as U is ramped up. As the interlayer potential broadens the bandwidth, it generally favors strong-coupling families with fewer fully occupied flavors, i.e., the FB family. This is consistent with the narrowing of the FI region in Fig. 12 as U increases. Beyond a threshold value of U, which is comparable across the filling factors, the phase diagram contains phases which cannot be understood as simple strong-coupling insulators. The flavor occupations and Chern numbers of these new phases are summarized in Table II.

TABLE II. Properties of phases at finite displacement field. The phases listed here appear in the finite displacement field phase diagrams of Fig. 12. $\widetilde{\text{FB}}$ represents the family that is obtained from the strong-coupling family FB via a displacement field-tuned topological transition. {flavor occ.} lists the flavor occupations in descending order. The Kekulé spiral (KS_κ) and charge density wave (CDW) can have fractional occupations due to intervalley coherence or translation symmetry breaking. C denotes the possible Chern numbers, with large bold entries corresponding to the dominant ground-state HF phases obtained in Fig. 12.

Phase/family	ν	{flavor occ.}	$\lvert C\rvert$
$\widetilde{\text{FB}}$	0	{1, 1, 1, 1}	**0**, **2**, 1
	1	{2, 1, 1, 1}	**0**, 1, 2
	2	{2, 2, 1, 1}	**0**, 1, 2
	3	{2, 2, 2, 1}	**0**, 1
KS_κ	1	{1.5, 1.5, 1, 1}	**0**
	2	{1.5, 1.5, 1.5, 1.5}	**0**
	3	{2, 2, 1.5, 1.5}	**0**
CDW	2	{1.5, 1.5, 1.5, 1.5}	**0**
	3	{2, 2, 1.5, 1.5}	**0**, **2**

For most values of θ, the first non-strong-coupling phase that is encountered as U increases is the $\widetilde{\text{FB}}$ family. The HF solution in this region shares the same symmetries and similar Chern basis occupations as the neighboring FB phase at smaller U. When entering the transition from the FB phase (which is restricted to $\theta \lesssim 1.8°$ for $\nu \neq 3$), the gap is greatly suppressed, implying a continuous or weakly first-order transition (which is the case within our HF calculations). However, the $\widetilde{\text{FB}}$ family possesses a distinct set of possible Chern numbers, which can be seen by comparing Tables I and II.

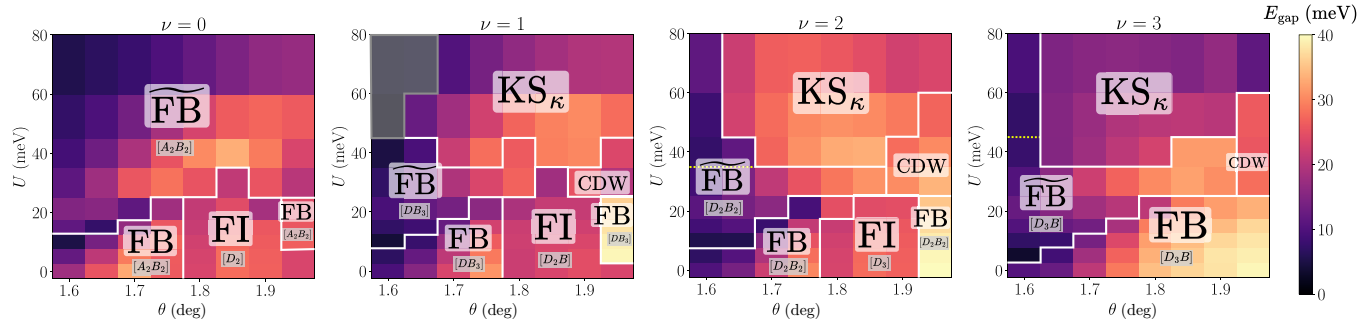

FIG. 12. Phase diagrams for non-negative integer fillings ν at finite displacement field. Color plot shows the Hartree-Fock band gap E_{gap}. White lines indicate approximate phase boundaries, shaded gray areas denote absence of a charge gap, and dotted yellow lines indicate a weak-coupling excitonic instability. For the translation-invariant phases, we also describe the dominant flavor-sublattice occupations of the lowest-energy HF solution, as in Fig. 5. Properties of the phases at finite displacement field are listed in Table II. System size is 12×12, $\epsilon_r = 8$, and $w_{AA} = 75\,\text{meV}$. CDW, charge density wave; KS_κ, Kekulé spiral.

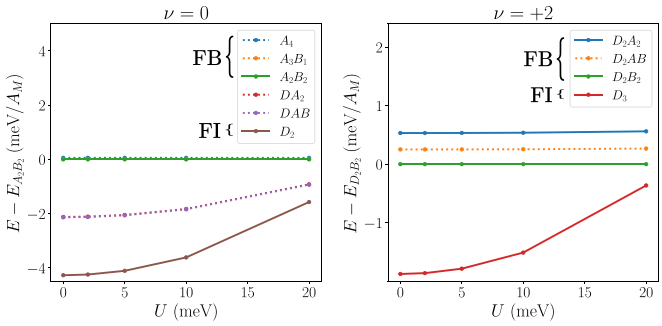

FIG. 13. Energetic competition between strong-coupling phases at finite displacement field. Self-consistent HF energies of different strong-coupling classes. Labeling is the same as Fig. 6. System size is 12×12, $\theta = 1.8°$, and $w_{AA} = 70$ meV.

Figure 14(a) reveals that this arises from a topological phase transition at the mBZ corners, using a state in the $[D_3B]$ class at $\nu = +3$ as an example. In this calculation, the empty conduction band is primarily composed of the $(\bar{K}, \downarrow, A)$ Chern band. As U increases, the energy of the B sublattice in the valence band for the $\bar{K}, \downarrow$ flavor sector rapidly increases and closes the gap at κ'. Across the topological transition, the bands get inverted so that the conduction band becomes topologically trivial, but the bands largely retain their original flavor and sublattice polarized character elsewhere in momentum space. Figure 14(b) demonstrates that the gap at the band closing point is sharply suppressed for the other fillings as well, with the threshold field decreasing slightly with density. The possible Chern numbers of the $\widetilde{\text{FB}}$ family in Table II are obtained by using a new effective set of sublattice Chern numbers $C_{K,s,A} = 0, C_{K,s,B} = -1, C_{\bar{K},s,A} = 0, C_{\bar{K},s,B} = 1$ [see Eq. (3)]. Figure 14(c) shows that the gap minimum is reduced for smaller twist angles. Hence, the system realizes a set of displacement field-tuned topological transitions, which we emphasize occur in the strongly interacting regime where there is still significant generalized flavor-sublattice ferromagnetism. We comment that the asymmetry and discontinuity of the HF gap about the transition point are similar to those seen in studies of the inverted charge transfer mechanism relevant for transition metal dichalcogenide heterobilayers [91], which also realizes a topological band inversion in the strongly interacting regime.

As in the low-U regime, there is a close energetic competition in the $\widetilde{\text{FB}}$ phase between classes which share the same flavor occupation numbers but differ in the sublattice polarizations. For larger U, these states can also become unstable to a weak-coupling excitonic instability.

Experimentally, the topological transitions would manifest as a dip in the resistive peak or incompressibility as a function of displacement field. Furthermore, since the phases below/above the transition have generically different Chern numbers, another signature would be a change in the anomalous Hall effect at the transition, as well as differing slopes of various features in the ν-B plane.

For all nonzero integer fillings, the system enters the Kekulé spiral (KS_κ) phase for sufficiently large interlayer potentials. This state shares some commonalities with the

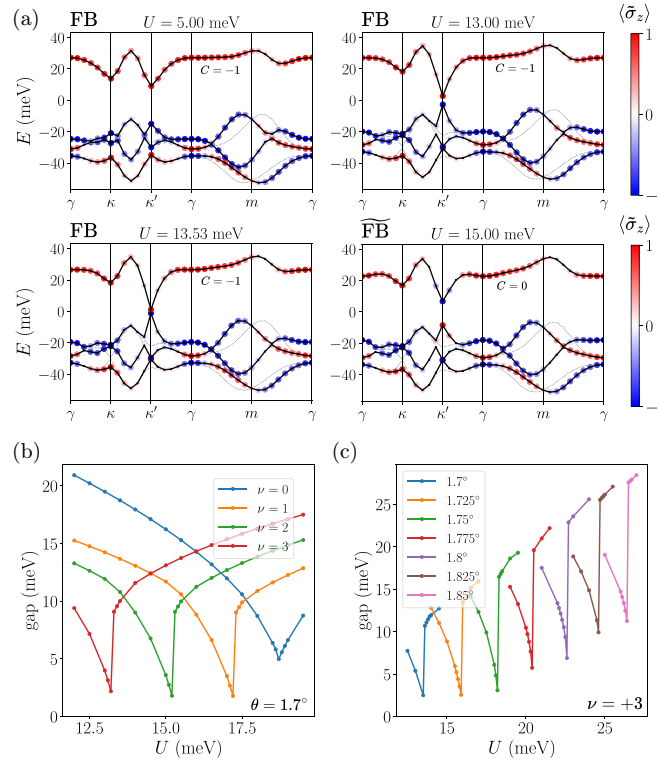

FIG. 14. Displacement field tuned topological transition. (a) First three plots show the HF band structures for the D_3B phase at $\nu = +3$ [see Fig. 9(a) for a schematic] for increasing interlayer potential U. For sufficiently large U, the system undergoes a topological transition in valley $\bar{K}$ to a phase where the conduction band no longer has a nonzero Chern number C. Colored dots indicate the Chern-sublattice polarization. Only the bands in the partially occupied spin sector are shown. System size is 18×18, $\theta = 1.7°$, and $w_{AA} = 75$ meV. (b) Gap vs U for different fillings ν at $\theta = 1.7°$. (c) Gap vs U for different twist angles at $\nu = +3$.

incommensurate Kekulé spiral (IKS) order which has been theoretically proposed [28–30] and experimentally observed in TBG [26] and mirror-symmetric trilayer graphene [52]. The KS_κ state preserves TRS $\hat{\mathcal{T}}$ but breaks moiré translation symmetry $\hat{T}_{\boldsymbol{a}_i}$ and valley $U(1)_v$. The flavor occupations (Table II) and lack of significant polarization in the Chern-sublattice further distinguish this state from the strong-coupling phases or their descendants obtained via excitonic instabilities or topological transitions. However, the KS_κ state preserves a twisted translation symmetry $\hat{T}'_{\boldsymbol{a}_i} = \hat{T}_{\boldsymbol{a}_i} e^{-i\frac{\boldsymbol{q}\boldsymbol{a}_i}{2}\tau_z}$ which includes a valley rotation. This property derives from the structure of the density matrix in the intervalley channel, where $P_{\boldsymbol{k}K;\boldsymbol{k}'\bar{K}}$ is forced to be zero unless $\boldsymbol{k}' = \boldsymbol{k} + \boldsymbol{q}$. The stabilization of this phase is traced to the momentum dependence of the dispersion for large U. By "boosting" the $\bar{K}$ valley by the Kekulé spiral wave vector $\boldsymbol{q}$ [Fig. 15(b)], the low- and high-energy features in the two valleys can be superposed according to the "lobe" principle described in Ref. [28]. As shown in Fig. 15, the shape of the noninteracting bands is imprinted on the resulting valley polarization of the HF bands. In contrast to the $\hat{C}_{2z}$-symmetric IKS which was originally proposed in the context of $\hat{C}_{3z}$-breaking heterostrain, the wave vector of the KS_κ appears to be pinned to one of the $\hat{C}_{3z}$-symmetric

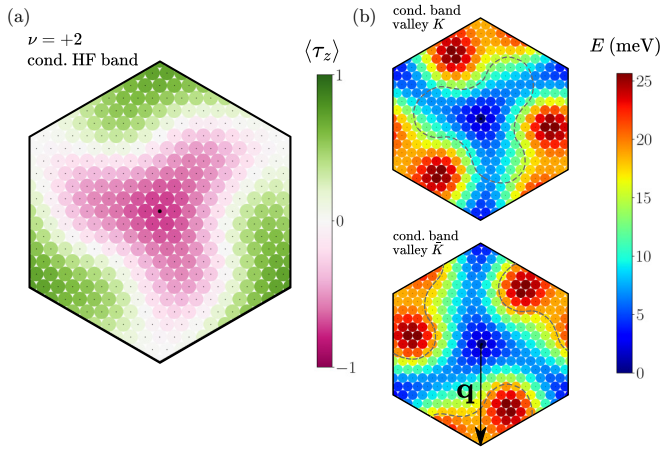

FIG. 15. Kekulé spiral (KS_κ) phase at finite displacement field. (a) Valley polarization $\langle \tau_z \rangle$ for the HF conduction band at $\nu = +2$ in one spin sector [the system is $SU_S(2)$ symmetric]. The momentum is measured using the original mBZ coordinates in valley K ($\tau_z = +1$). (b) Noninteracting dispersion of the BM conduction bands in both valleys. Dashed contour in valley $\bar{K}$ roughly indicates the high-energy lobe there. The same contour is shown in K, but shifted by $-\boldsymbol{q}$, where $\boldsymbol{q}$ is the Kekulé spiral wave vector. In the KS_κ phase, any intervalley coherence hybridizes a momentum $\boldsymbol{k}$ in K with $\boldsymbol{k}+\boldsymbol{q}$ in $\bar{K}$. The κ subscript indicates that $\boldsymbol{q}$ lies at one of the C_3-symmetric momenta κ or κ'. System size is 18×18, $\theta = 1.8^\circ$, $w_{AA} = 75\,\mathrm{meV}$, $U = 50\,\mathrm{meV}$.

corners of the mBZ, and the lobes have a sizable sublattice polarization. The preservation of $\hat{C}_{3z}$ symmetry, the lack of $\hat{C}_{2z}$, and the emergence at finite D suggest that the KS_κ is more closely connected to the "commensurate Kekulé spiral order" recently uncovered in HF studies of mirror-symmetric trilayer graphene in Ref. [92]. The KS_κ state is difficult to experimentally discriminate from the $C = 0$ members of the $\widetilde{\mathrm{FB}}$ phase. The most direct test would be observation of significant correlation-induced Kekulé distortion on the graphene scale using STM [26,52], since none of the other candidate phases have an appreciable amount of intervalley coherence.

Finally at larger angles, there is a small sliver of the phase diagram which consists of a CDW on the moiré scale that breaks TRS even in the absence of valley polarization. The TSB occurs predominantly in the B sublattice which takes advantage of the dispersive momentum features by folding the bands. This quadruples the unit-cell area because the periodicity along both moiré axes is doubled. At $\nu = +2$, the sublattice basis occupations are consistent with starting from an $[A_4]$ state and occupying half a B band in each flavor.

VI. DISCUSSION

At low displacement fields, as well as intermediate fields (the $\widetilde{\mathrm{FB}}$ phase), our findings paint a picture of a multitude of closely competing (near)-strong-coupling states with contrasting flavor and sublattice polarizations, and varying electronic topology. A key question is how this manifold is ultimately split, which is relevant for resolving the low-temperature physics. Different strong-coupling classes within the same family (see Fig. 4 for a schematic of labeling of strong-coupling states) have similar energies within 1 meV per moiré cell as illustrated in Fig. 6 and anticipated from strong-coupling theory (Sec. III). While the HF calculations and strong-coupling analysis show a consistent preference towards maximizing the occupation of the B bands for $\nu \gtrsim 0$, the splittings are small enough that they could be reversed by effects not captured in our modeling like residual coupling to the hBN substrate. Within a given strong-coupling class, the remaining choice of the state pertains to the flavor degrees of freedom. As an example, consider the $[D_2B_2]$ class of the FB family at $\nu = +2$—a particular state can be chosen by specifying the valley and spin quantum numbers of the two unoccupied A bands. Some degeneracies are expected to remain exact, such as the global $SU(2)_S$ spin symmetry or spinless time reversal $\hat{\mathcal{T}}$, unless they are deliberately broken with, e.g., an external magnetic field. Others are only exact because certain terms have been neglected from the Hamiltonian in our paper. These include various Hund couplings which are not invariant under independent spin rotations in the two valleys. If we assign one empty A band to each valley, then their spins will align (antialign) if the correction is ferromagnetic (antiferromagnetic). The sign of the Hund term involves opposite contributions from optical phonons and intervalley Coulomb scattering, and is difficult to pin down theoretically [75], though there is experimental evidence that this is antiferromagnetic in TBG [93].

As discussed in detail in Sec. III, there is another type of degeneracy which is unique to the mean-field nature of Hartree-Fock, and corresponds to acting with the spinless time-reversal operation only for one spin projection. For the $[D_2B_2]$ class at $\nu = +2$, a scenario where this applies is where the empty A bands have flavors $(K,\uparrow)$ and $(\bar{K},\downarrow)$, vs $(K,\uparrow)$ and $(K,\downarrow)$. Crucially, these two choices have $|C| = 0$ and 2 respectively, but are degenerate in our calculations since the HF Hamiltonian is quadratic. Furthermore, this degeneracy is also not split to lowest order in the strong-coupling perturbation theory of Sec. III. However, "time reversal in one spin projection" cannot be an exact symmetry since it is neither unitary nor antiunitary. Therefore, quantum fluctuations which introduce deviations from a single Slater determinant will split this degeneracy. These "Hartree-Fock symmetries" also occur to a limited extent in other moiré systems like TBG [28,94], so an interesting future direction is to systematically investigate how the corresponding degeneracies are lifted.

The small energy differences between different classes and families of strong-coupling states can be traced to the perturbative proximity to the chiral-flat strong-coupling limit, where all generalized ferromagnets are split only by a small amount corresponding to the sublattice polarization [Eq. (6)]. In TBG, this close competition is sidestepped in many devices by the presence of heterostrain [22–25], which allows the IKS to undercut the strong-coupling manifold [26,28–30,52]. It would be useful to investigate the effect that strain has on the band structure [95,96] and phase diagram of h-HTG. We anticipate that it is less susceptible to strain-induced IKS order, since the larger twist angle enhances the interaction scale, and the homogeneous charge density reduces the tendency to form significant momentum-dependent features in the interacting band structure. Owing to the supermoiré structure,

strain could also influence or be absorbed into the relaxation of domains in a nontrivial fashion [42]. We note though that the related KS_κ state appears to emerge for moderate displacement fields already in the absence of strain (Fig. 12)—it would be interesting to check whether this persists with more sophisticated numerical techniques like density matrix renormalization group (DMRG) [30,97].

We restrict our numerical calculations to non-negative integer fillings due to the exact particle-hole symmetry we impose on the model. However, it is known that in other systems for which particle-hole symmetry is commonly assumed theoretically, the experimental data show pronounced particle-hole asymmetry in fundamental observables like the positions of the dominant correlated insulators and superconducting domes (see for instance Ref. [98]). We anticipate that similar considerations will apply to our system, and that refinements to the theoretical modeling that aim to cure this deficiency, e.g., by adding terms to the continuum model [64,67,99–101], could be applied to h-HTG.

While we have focused on the integer phase diagrams, our results influence the physics at noninteger fillings. At low dopings away from integer ν, the Fermi surfaces are likely controlled by the interacting band structure of the parent insulator. Information on the number of Fermi surfaces and their sizes is invaluable since it can be extracted via measurements of the Landau fans and their degeneracies (though quantum oscillations may be hard to detect if the effective masses are too large). Consider for instance electron doping the particular $\nu = +2$ $[D_3]$ state shown in Fig. 7(b) at zero displacement field. The electrons initially form three $\hat{C}_{3z}$-related Fermi surfaces, and are predominantly of B character. Note that these conclusions may be altered in the presence of extrinsic $\hat{C}_{3z}$-breaking strain, or nematicity induced by polarizing in momentum space [102]. For other states, as discussed in Sec. IV for electron doping the $\nu = +3$ $[D_3B]$ insulator, the system may additionally undergo a finite-filling sublattice transition where some of the carriers abruptly switch from one sublattice to the other. This would truncate the Landau fans emanating from the parent integer, and lead to filling-dependent modulations in the spectral function in STM or scanning tunneling spectroscopy [80] or the electronic compressibility in SET [90] measurements. Pinning down the precise pattern of flavor/sublattice transitions and their corresponding signatures would require the HF computations to be extended to all noninteger fillings. Given that the B bands have larger dispersive features, we expect that a common driving force behind the sublattice transitions is a minimization of the kinetic energy of the B quasiparticles.

At fractional noninteger fillings, the system can form correlated insulators beyond simple flavor-symmetry-broken Fermi liquids. Accessible within HF are TSB phases obtained by folding the mBZ and inducing a moiré charge density wave. (Note that a modified Lieb-Schulz-Mattis theorem forbids a pure flavor spiral order from being gapped at noninteger filling [28].) As the B bands have significant momentum-dependent features, we expect the TSB order parameter to be concentrated here, as for the integer CDW phase in Fig. 12. Preliminary calculations show that this is indeed the case, and find various TSB insulators at various third and half fillings. We defer a detailed exploration of such phases to future work. As proposed in Ref. [42], another class of candidate states is fractional Chern insulators at, say, $\nu = 3 + \frac{1}{3}$ or $3 + \frac{2}{3}$. This scenario is motivated by the narrow quasiparticle dispersion, energetic isolation, and ideal quantum geometry [13,21,53,60,103–110] of the partially occupied A band (Fig. 9), and would need to be checked by DMRG [21] or exact diagonalization [111–113]. The modeling is simplified by the substantial suppression of interaction renormalization. Interesting correlated states have also been proposed for higher $|C| = 2$ bands [35,103,107,114–126], which could be relevant if the energetics at fractional fillings prefer that B bands are partially filled instead.

We expect that real samples of HTG will form a supermoiré pattern that locally relaxes into domains of h-HTG and its $\hat{C}_{2z}$-related partner $\bar{\text{h}}$-HTG [42], as illustrated in Fig. 1. The structure, as a whole, therefore has $\hat{C}_{2z}$ symmetry on the supermoiré scale, despite the symmetry being absent within the h-HTG structure. The Chern numbers of the sublattice basis in $\bar{\text{h}}$-HTG are obtained by taking $A \leftrightarrow B$ and $K \leftrightarrow \bar{K}$ in Eq. (3). Since the central bands in the two domains carry opposite valley Hall numbers, the domain walls induce a network of gapless topological edge modes that cross the remote band gap at $|\nu| = 4$, which can be traced via local imaging. The shape of this network is triangular in the pristine limit, but may deform due to factors such as twist angle disorder and strain. For other integer fillings, the correlated insulators in the h-HTG and $\bar{\text{h}}$-HTG will have experimental signatures in the form of resistance peaks, as well as signatures of the displacement-field tuned topological transition.

Furthermore, there is additional physics arising from the choice of correlated state in two adjacent domains [127,128]. Degeneracies within each domain can be split by the configuration in neighboring domains. As a concrete example, we consider the strong-coupling $[D_3B]$ class in h-HTG and the equivalent $[D_3A]$ class in $\bar{\text{h}}$-HTG at $\nu = +3$, which have $C = \pm 1$. Ignoring spin for simplicity, there is a freedom in assigning valleys to the unoccupied band in each domain [see schematic in Fig. 9(a)]. For equal (opposite) valleys, the domains have opposite (equal) Chern numbers, leading to co-propagating (counterpropagating) edge modes at the interface, and realizing Chern (valley) domain walls. While a detailed analysis of domain wall energetics is an important topic for future work, we argue that Chern domain walls should be favored at zero magnetic field. Relaxation calculations show that the aperiodic interface channels are only a few moiré lengths wide [42], suggesting that mutual exchange physics of the two domains, which is not possible between opposite valleys, is important. Furthermore, intervalley coherence is suppressed due to the mismatch of Chern numbers in the two valleys [39], which discourages spatial texturing of the valley wall. Hence, we anticipate that Chern domains will be energetically favored, thus resulting in a "Chern mosaic" [128] of h-HTG and $\bar{\text{h}}$-HTG domains carrying opposite Chern numbers. This possibility can be numerically tested with similar techniques as Ref. [127] and visualized using a superconducting quantum intereference device on tip [128,129]. A sufficiently strong perpendicular magnetic field may counteract this and induce valley domain walls, since it couples to the orbital magnetization of the domains.

Another important question is the consequence of such Chern domain physics in transport. Even when the h-HTG and $\bar{\text{h}}$-HTG domains individually realize Chern insulators, thus breaking $\mathcal{T}$, it is possible that $\hat{C}_{2z}\mathcal{T}$ is restored at the supermoiré scale, as is the case for the above Chern mosaic. We remark that this supermoiré scale $\hat{C}_{2z}\mathcal{T}$ symmetric Chern mosaic is unique to HTG, and is absent in hBN-aligned TBG [128,130]. The presence of $\hat{C}_{2z}\mathcal{T}$ forbids a nonzero net Hall conductivity in the thermodynamic limit. However, this vanishing Hall conductivity relies on the precise cancellation of currents in h-HTG and $\bar{\text{h}}$-HTG domains, which are potentially several hundred nanometers wide and spatially separated. Because of this, extrinsic effects in real mesoscopic devices, such as various forms of strain or twist angle disorder (which can vary greatly on the micrometer scale), the precise placement of contacts with respect to the domains, or boundary effects on the domain sizes and shapes, likely mean that the supermoiré scale $\hat{C}_{2z}\mathcal{T}$ symmetry is not relevant to electronic transport properties at experimentally relevant scales. Hence, we expect a remnant (nonquantized) anomalous Hall effect to be experimentally measurable even in the Chern mosaic state, reflecting the broken $\mathcal{T}$ symmetry. Experimental determination of the Chern numbers can be achieved using the Streda formula in a finite magnetic field. Local techniques leveraging STM [26,34,52,80–84] and SET [38,85,86] are able to resolve this information within each domain.

If all domains have the same Chern number, the possibility of detecting a quantized Hall effect using a global transport measurement turns on the details of the edge modes. Assuming $U(1)$ spin and valley symmetries, there are no protected gapless edge modes only if the domains share the same Chern numbers within each flavor. As discussed in Appendix D of Ref. [77], the determination of the valley Chern number needs to be performed carefully, and we find that the only strong-coupling states that do not necessarily host protected edge modes between h-HTG and $\bar{\text{h}}$-HTG domains are the ones at charge neutrality.

In conclusion, we have presented a comprehensive analysis of the interacting physics at integer fillings of HTG using complementary methods of strong-coupling theory and HF. Our analysis reveals h-HTG as an ideal platform for realizing strong-coupling physics, with interactions dominating over bandwidth at all integer fillings. We uncover a rich hierarchy of correlated insulating states, many of which are topological, and predict topological phase transitions as a function of displacement field. We discuss in detail the experimental ramifications of our findings, which can be readily tested with existing experimental techniques. Our paper paints a rich picture of moiré-scale interaction-driven topology intertwined with the supermoiré scale topological domains, paving the way for future studies of interacting physics in HTG.

ACKNOWLEDGMENTS

We thank Ashvin Vishwanath and Ben Feldman for valuable comments on the paper. T.D. and Y.K. thank Liqiao Xia, Aviram Uri, Sergio de la Barrera, Ziyan Zhu, Liang Fu, and Pablo Jarillo-Herrero for valuable discussions and collaboration on related projects. Y.K. thanks Glenn Wagner for previous collaboration on the Hartree-Fock code. P.L. thanks Eslam Khalaf and Ashvin Vishwanath for valuable discussions and previous collaboration on related projects. T.D. acknowledges support from a startup fund at Stanford University. C.F.B.L. was supported by the National Science Foundation Graduate Research Fellowship under Grant No. 1745303.

[1] D. C. Tsui, H. L. Stormer, and A. C. Gossard, Two-dimensional magnetotransport in the extreme quantum limit, Phys. Rev. Lett. **48**, 1559 (1982).

[2] S. M. Girvin, The quantum Hall effect: Novel excitations and broken symmetries, in *Aspects Topologiques de la Physique en Basse Dimension. Topological Aspects of Low Dimensional Systems: Session LXIX. 7–31 July 1998* (Springer, New York, 2002), pp. 53–175.

[3] J. Eisenstein, Exciton condensation in bilayer quantum Hall systems, Annu. Rev. Condens. Matter Phys. **5**, 159 (2014).

[4] M. O. Goerbig, Electronic properties of graphene in a strong magnetic field, Rev. Mod. Phys. **83**, 1193 (2011).

[5] Y. Cao, V. Fatemi, A. Demir, S. Fang, S. L. Tomarken, J. Y. Luo, J. D. Sanchez-Yamagishi, K. Watanabe, T. Taniguchi, E. Kaxiras, R. C. Ashoori, and P. Jarillo-Herrero, Correlated insulator behaviour at half-filling in magic-angle graphene superlattices, Nature (London) **556**, 80 (2018).

[6] Y. Cao, V. Fatemi, S. Fang, K. Watanabe, T. Taniguchi, E. Kaxiras, and P. Jarillo-Herrero, Unconventional superconductivity in magic-angle graphene superlattices, Nature (London) **556**, 43 (2018).

[7] M. Yankowitz, S. Chen, H. Polshyn, Y. Zhang, K. Watanabe, T. Taniguchi, D. Graf, A. F. Young, and C. R. Dean, Tuning superconductivity in twisted bilayer graphene, Science **363**, 1059 (2019).

[8] X. Lu, P. Stepanov, W. Yang, M. Xie, M. A. Aamir, I. Das, C. Urgell, K. Watanabe, T. Taniguchi, G. Zhang *et al.*, Superconductors, orbital magnets and correlated states in magic-angle bilayer graphene, Nature (London) **574**, 653 (2019).

[9] E. Y. Andrei, D. K. Efetov, P. Jarillo-Herrero, A. H. MacDonald, K. F. Mak, T. Senthil, E. Tutuc, A. Yazdani, and A. F. Young, The marvels of moiré materials, Nat. Rev. Mater. **6**, 201 (2021).

[10] K. F. Mak and J. Shan, Semiconductor moiré materials, Nat. Nanotechnol. **17**, 686 (2022).

[11] N. Bultinck, E. Khalaf, S. Liu, S. Chatterjee, A. Vishwanath, and M. P. Zaletel, Ground state and hidden symmetry of magic-angle graphene at even integer filling, Phys. Rev. X **10**, 031034 (2020).

[12] B. Lian, Z.-D. Song, N. Regnault, D. K. Efetov, A. Yazdani, and B. A. Bernevig, TBG IV: Exact insulator ground states and phase diagram of twisted bilayer graphene, Phys. Rev. B **103**, 205414 (2021).

[13] P. J. Ledwith, E. Khalaf, and A. Vishwanath, Strong coupling theory of magic-angle graphene: A pedagogical introduction, Ann. Phys. (NY) **435**, 168646 (2021).

[14] G. Tarnopolsky, A. J. Kruchkov, and A. Vishwanath, Origin of magic angles in twisted bilayer graphene, Phys. Rev. Lett. **122**, 106405 (2019).

[15] F. Guinea and N. R. Walet, Electrostatic effects, band distortions, and superconductivity in twisted graphene bilayers, Proc. Natl. Acad. Sci. USA **115**, 13174 (2018).

[16] L. Rademaker, D. A. Abanin, and P. Mellado, Charge smoothening and band flattening due to hartree corrections in twisted bilayer graphene, Phys. Rev. B **100**, 205114 (2019).

[17] T. Cea, N. R. Walet, and F. Guinea, Electronic band structure and pinning of fermi energy to van hove singularities in twisted bilayer graphene: A self-consistent approach, Phys. Rev. B **100**, 205113 (2019).

[18] Z. A. Goodwin, V. Vitale, X. Liang, A. A. Mostofi, and J. Lischner, Hartree theory calculations of quasiparticle properties in twisted bilayer graphene, Electron. Struct. **2**, 034001 (2020).

[19] J. Kang, B. A. Bernevig, and O. Vafek, Cascades between light and heavy fermions in the normal state of magic-angle twisted bilayer graphene, Phys. Rev. Lett. **127**, 266402 (2021).

[20] A. T. Pierce, Y. Xie, J. M. Park, E. Khalaf, S. H. Lee, Y. Cao, D. E. Parker, P. R. Forrester, S. Chen, K. Watanabe *et al.*, Unconventional sequence of correlated chern insulators in magic-angle twisted bilayer graphene, Nat. Phys. **17**, 1210 (2021).

[21] D. Parker, P. Ledwith, E. Khalaf, T. Soejima, J. Hauschild, Y. Xie, A. Pierce, M. P. Zaletel, A. Yacoby, and A. Vishwanath, Field-tuned and zero-field fractional Chern insulators in magic angle graphene, arXiv:2112.13837.

[22] A. Kerelsky, L. J. McGilly, D. M. Kennes, L. Xian, M. Yankowitz, S. Chen, K. Watanabe, T. Taniguchi, J. Hone, C. Dean *et al.*, Maximized electron interactions at the magic angle in twisted bilayer graphene, Nature (London) **572**, 95 (2019).

[23] Y. Choi, J. Kemmer, Y. Peng, A. Thomson, H. Arora, R. Polski, Y. Zhang, H. Ren, J. Alicea, G. Refael *et al.*, Electronic correlations in twisted bilayer graphene near the magic angle, Nat. Phys. **15**, 1174 (2019).

[24] Y. Xie, B. Lian, B. Jäck, X. Liu, C.-L. Chiu, K. Watanabe, T. Taniguchi, B. A. Bernevig, and A. Yazdani, Spectroscopic signatures of many-body correlations in magic-angle twisted bilayer graphene, Nature (London) **572**, 101 (2019).

[25] F. Mesple, A. Missaoui, T. Cea, L. Huder, F. Guinea, G. Trambly de Laissardière, C. Chapelier, and V. T. Renard, Heterostrain determines flat bands in magic-angle twisted graphene layers, Phys. Rev. Lett. **127**, 126405 (2021).

[26] K. P. Nuckolls, R. L. Lee, M. Oh, D. Wong, T. Soejima, J. P. Hong, D. Călugăru, J. Herzog-Arbeitman, B. A. Bernevig, K. Watanabe *et al.*, Quantum textures of the many-body wavefunctions in magic-angle graphene, Nature (London) **620**, 525 (2023).

[27] D. E. Parker, T. Soejima, J. Hauschild, M. P. Zaletel, and N. Bultinck, Strain-induced quantum phase transitions in magic-angle graphene, Phys. Rev. Lett. **127**, 027601 (2021).

[28] Y. H. Kwan, G. Wagner, T. Soejima, M. P. Zaletel, S. H. Simon, S. A. Parameswaran, and N. Bultinck, Kekulé spiral order at all nonzero integer fillings in twisted bilayer graphene, Phys. Rev. X **11**, 041063 (2021).

[29] G. Wagner, Y. H. Kwan, N. Bultinck, S. H. Simon, and S. A. Parameswaran, Global phase diagram of the normal state of twisted bilayer graphene, Phys. Rev. Lett. **128**, 156401 (2022).

[30] T. Wang, D. E. Parker, T. Soejima, J. Hauschild, S. Anand, N. Bultinck, and M. P. Zaletel, Ground-state order in magic-angle graphene at filling $\nu = -3$: A full-scale density matrix renormalization group study, Phys. Rev. B **108**, 235128 (2023).

[31] M. Serlin, C. L. Tschirhart, H. Polshyn, Y. Zhang, J. Zhu, K. Watanabe, T. Taniguchi, L. Balents, and A. F. Young, Intrinsic quantized anomalous Hall effect in a moiré heterostructure, Science **367**, 900 (2020).

[32] A. L. Sharpe, E. J. Fox, A. W. Barnard, J. Finney, K. Watanabe, T. Taniguchi, M. A. Kastner, and D. Goldhaber-Gordon, Emergent ferromagnetism near three-quarters filling in twisted bilayer graphene, Science **365**, 605 (2019).

[33] P. Stepanov, M. Xie, T. Taniguchi, K. Watanabe, X. Lu, A. H. MacDonald, B. A. Bernevig, and D. K. Efetov, Competing zero-field Chern insulators in superconducting twisted bilayer graphene, Phys. Rev. Lett. **127**, 197701 (2021).

[34] K. P. Nuckolls, M. Oh, D. Wong, B. Lian, K. Watanabe, T. Taniguchi, B. A. Bernevig, and A. Yazdani, Strongly correlated Chern insulators in magic-angle twisted bilayer graphene, Nature (London) **588**, 610 (2020).

[35] Y.-L. Wu, N. Regnault, and B. A. Bernevig, Bloch model wave functions and pseudopotentials for all fractional Chern insulators, Phys. Rev. Lett. **110**, 106802 (2013).

[36] I. Das, X. Lu, J. Herzog-Arbeitman, Z.-D. Song, K. Watanabe, T. Taniguchi, B. A. Bernevig, and D. K. Efetov, Symmetry-broken Chern insulators and Rashba-like Landau-level crossings in magic-angle bilayer graphene, Nat. Phys. **17**, 710 (2021).

[37] Y. Saito, J. Ge, L. Rademaker, K. Watanabe, T. Taniguchi, D. A. Abanin, and A. F. Young, Hofstadter subband ferromagnetism and symmetry-broken Chern insulators in twisted bilayer graphene, Nat. Phys. **17**, 478 (2021).

[38] Y. Xie, A. T. Pierce, J. M. Park, D. E. Parker, E. Khalaf, P. Ledwith, Y. Cao, S. H. Lee, S. Chen, P. R. Forrester, K. Watanabe, T. Taniguchi, A. Vishwanath, P. Jarillo-Herrero, and A. Yacoby, Fractional Chern insulators in magic-angle twisted bilayer graphene, Nature (London) **600**, 439 (2021).

[39] N. Bultinck, S. Chatterjee, and M. P. Zaletel, Mechanism for anomalous Hall ferromagnetism in twisted bilayer graphene, Phys. Rev. Lett. **124**, 166601 (2020).

[40] Y.-H. Zhang, D. Mao, Y. Cao, P. Jarillo-Herrero, and T. Senthil, Nearly flat Chern bands in moiré superlattices, Phys. Rev. B **99**, 075127 (2019).

[41] J. Liu, J. Liu, and X. Dai, Pseudo Landau level representation of twisted bilayer graphene: Band topology and implications on the correlated insulating phase, Phys. Rev. B **99**, 155415 (2019).

[42] T. Devakul, P. J. Ledwith, L.-Q. Xia, A. Uri, S. C. de la Barrera, P. Jarillo-Herrero, and L. Fu, Magic-angle helical trilayer graphene, Sci. Adv. **9**, eadi6063 (2023).

[43] C. Mora, N. Regnault, and B. A. Bernevig, Flatbands and perfect metal in trilayer moiré graphene, Phys. Rev. Lett. **123**, 026402 (2019).

[44] Z. Zhu, S. Carr, D. Massatt, M. Luskin, and E. Kaxiras, Twisted trilayer graphene: A precisely tunable platform for correlated electrons, Phys. Rev. Lett. **125**, 116404 (2020).

[45] Y. Mao, D. Guerci, and C. Mora, Supermoiré low-energy effective theory of twisted trilayer graphene, Phys. Rev. B **107**, 125423 (2023).

[46] F. K. Popov and G. Tarnopolsky, Magic angles in equal-twist trilayer graphene, arXiv:2303.15505.
[47] D. Guerci, Y. Mao, and C. Mora, Chern mosaic and ideal flat bands in equal-twist trilayer graphene, arXiv:2305.03702.
[48] N. Nakatsuji, T. Kawakami, and M. Koshino, Multiscale lattice relaxation in general twisted trilayer graphenes, Phys. Rev. X **13**, 041007 (2023).
[49] F. K. Popov and G. Tarnopolsky, Magic angle butterfly in twisted trilayer graphene, Phys. Rev. Res. **5**, 043079 (2023).
[50] D. C. W. Foo, Z. Zhan, M. M. A. Ezzi, L. Peng, S. Adam, and F. Guinea, Extended magic phase in twisted graphene multilayers, Phys. Rev. Res. **6**, 013165 (2024).
[51] D. Guerci, Y. Mao, and C. Mora, Nature of even and odd magic angles in helical twisted trilayer graphene, arXiv:2308.02638.
[52] H. Kim, Y. Choi, Étienne Lantagne-Hurtubise, C. Lewandowski, A. Thomson, L. Kong, H. Zhou, E. Baum, Y. Zhang, L. Holleis, K. Watanabe, T. Taniguchi, A. F. Young, J. Alicea, and S. Nadj-Perge, Imaging inter-valley coherent order in magic-angle twisted trilayer graphene, arXiv:2304.10586.
[53] S. A. Parameswaran, R. Roy, and S. L. Sondhi, Fractional quantum Hall physics in topological flat bands, C. R. Phys. **14**, 816 (2013).
[54] E. J. Bergholtz and Z. Liu, Topological flat band models and fractional Chern insulators, Int. J. Mod. Phys. B **27**, 1330017 (2013).
[55] Z. Liu and E. J. Bergholtz, Recent developments in fractional Chern insulators, Encyclo. Condens. Matter Phys. **1**, 515 (2023).
[56] T. Neupert, L. Santos, C. Chamon, and C. Mudry, Fractional quantum Hall states at zero magnetic field, Phys. Rev. Lett. **106**, 236804 (2011).
[57] D. Sheng, Z.-C. Gu, K. Sun, and L. Sheng, Fractional quantum Hall effect in the absence of Landau levels, Nat. Commun. **2**, 389 (2011).
[58] N. Regnault and B. A. Bernevig, Fractional Chern insulator, Phys. Rev. X **1**, 021014 (2011).
[59] T. Scaffidi and G. Möller, Adiabatic continuation of fractional Chern insulators to fractional quantum hall states, Phys. Rev. Lett. **109**, 246805 (2012).
[60] R. Roy, Band geometry of fractional topological insulators, Phys. Rev. B **90**, 165139 (2014).
[61] S. Kourtis, T. Neupert, C. Chamon, and C. Mudry, Fractional Chern insulators with strong interactions far exceeding bandgaps, Phys. Rev. Lett. **112**, 126806 (2014).
[62] R. Bistritzer and A. H. MacDonald, Moiré bands in twisted double-layer graphene, Proc. Natl. Acad. Sci. USA **108**, 12233 (2011).
[63] N. N. T. Nam and M. Koshino, Lattice relaxation and energy band modulation in twisted bilayer graphene, Phys. Rev. B **96**, 075311 (2017).
[64] S. Carr, S. Fang, Z. Zhu, and E. Kaxiras, Exact continuum model for low-energy electronic states of twisted bilayer graphene, Phys. Rev. Res. **1**, 013001 (2019).
[65] O. Vafek and J. Kang, Renormalization group study of hidden symmetry in twisted bilayer graphene with Coulomb interactions, Phys. Rev. Lett. **125**, 257602 (2020).
[66] S. Carr, D. Massatt, S. B. Torrisi, P. Cazeaux, M. Luskin, and E. Kaxiras, Relaxation and domain formation in incommensurate two-dimensional heterostructures, Phys. Rev. B **98**, 224102 (2018).
[67] F. Guinea and N. R. Walet, Continuum models for twisted bilayer graphene: Effect of lattice deformation and hopping parameters, Phys. Rev. B **99**, 205134 (2019).
[68] P. J. Ledwith, E. Khalaf, Z. Zhu, S. Carr, E. Kaxiras, and A. Vishwanath, TB or not TB? Contrasting properties of twisted bilayer graphene and the alternating twist n-layer structures ($n = 3, 4, 5, \ldots$), arXiv:2111.11060.
[69] M. Koshino and N. N. T. Nam, Effective continuum model for relaxed twisted bilayer graphene and moiré electron-phonon interaction, Phys. Rev. B **101**, 195425 (2020).
[70] M. Koshino, N. F. Q. Yuan, T. Koretsune, M. Ochi, K. Kuroki, and L. Fu, Maximally localized Wannier orbitals and the extended Hubbard model for twisted bilayer graphene, Phys. Rev. X **8**, 031087 (2018).
[71] A. Uri, S. C. de la Barrera, M. T. Randeria, D. Rodan-Legrain, T. Devakul, P. J. Crowley, N. Paul, K. Watanabe, T. Taniguchi, R. Lifshitz *et al.*, Superconductivity and strong interactions in a tunable moiré quasiperiodic crystal, Nature **620**, 762 (2023).
[72] E. Khalaf, S. Chatterjee, N. Bultinck, M. P. Zaletel, and A. Vishwanath, Charged skyrmions and topological origin of superconductivity in magic-angle graphene, Sci. Adv. **7**, eabf5299 (2021).
[73] M. Xie and A. H. MacDonald, Nature of the correlated insulator states in twisted bilayer graphene, Phys. Rev. Lett. **124**, 097601 (2020).
[74] Y. H. Kwan, G. Wagner, N. Bultinck, S. H. Simon, and S. A. Parameswaran, Skyrmions in twisted bilayer graphene: Stability, pairing, and crystallization, Phys. Rev. X **12**, 031020 (2022).
[75] S. Chatterjee, N. Bultinck, and M. P. Zaletel, Symmetry breaking and skyrmionic transport in twisted bilayer graphene, Phys. Rev. B **101**, 165141 (2020).
[76] E. Cancès and C. Le Bris, Can we outperform the diis approach for electronic structure calculations?, Int. J. Quantum Chem. **79**, 82 (2000).
[77] See Supplemental Material at http://link.aps.org/supplemental/10.1103/PhysRevB.109.125141 for more details of the strong coupling perturbation theory, flavor permutation symmetry and valley Chern number.
[78] O. Vafek and J. Kang, Lattice model for the coulomb interacting chiral limit of magic-angle twisted bilayer graphene: Symmetries, obstructions, and excitations, Phys. Rev. B **104**, 075143 (2021).
[79] B. A. Bernevig, Z. Song, N. Regnault, and B. Lian, TBG III: Interacting Hamiltonian and exact symmetries of twisted bilayer graphene, Phys. Rev. B **103**, 205413 (2021).
[80] D. Wong, K. P. Nuckolls, M. Oh, B. Lian, Y. Xie, S. Jeon, K. Watanabe, T. Taniguchi, B. A. Bernevig, and A. Yazdani, Cascade of electronic transitions in magic-angle twisted bilayer graphene, Nature (London) **582**, 198 (2020).
[81] Y. Choi, H. Kim, Y. Peng, A. Thomson, C. Lewandowski, R. Polski, Y. Zhang, H. S. Arora, K. Watanabe, T. Taniguchi *et al.*, Correlation-driven topological phases in magic-angle twisted bilayer graphene, Nature (London) **589**, 536 (2021).
[82] Y. Choi, H. Kim, C. Lewandowski, Y. Peng, A. Thomson, R. Polski, Y. Zhang, K. Watanabe, T. Taniguchi, J. Alicea, and S. Nadj-Perge, Interaction-driven band flattening and correlated phases in twisted bilayer graphene, Nat. Phys. **17**, 1375 (2021).

[83] S. Turkel, J. Swann, Z. Zhu, M. Christos, K. Watanabe, T. Taniguchi, S. Sachdev, M. S. Scheurer, E. Kaxiras, C. R. Dean, and A. N. Pasupathy, Orderly disorder in magic-angle twisted trilayer graphene, Science **376**, 193 (2022).

[84] C. Zhang, T. Zhu, T. Soejima, S. Kahn, K. Watanabe, T. Taniguchi, A. Zettl, F. Wang, M. P. Zaletel, and M. F. Crommie, Local spectroscopy of a gate-switchable moiré quantum anomalous Hall insulator, Nat. Commun. **14**, 3595 (2023).

[85] J. Yu, B. A. Foutty, Z. Han, M. E. Barber, Y. Schattner, K. Watanabe, T. Taniguchi, P. Phillips, Z.-X. Shen, S. A. Kivelson *et al.*, Correlated Hofstadter spectrum and flavour phase diagram in magic-angle twisted bilayer graphene, Nat. Phys. **18**, 825 (2022).

[86] J. Yu, B. A. Foutty, Y. H. Kwan, M. E. Barber, K. Watanabe, T. Taniguchi, Z.-X. Shen, S. A. Parameswaran, and B. E. Feldman, Spin skyrmion gaps as signatures of intervalley-coherent insulators in magic-angle twisted bilayer graphene, Nat. Commun. **14**, 6679 (2023).

[87] J. Kang and O. Vafek, Non-Abelian Dirac node braiding and near-degeneracy of correlated phases at odd integer filling in magic-angle twisted bilayer graphene, Phys. Rev. B **102**, 035161 (2020).

[88] Z.-D. Song and B. A. Bernevig, Magic-angle twisted bilayer graphene as a topological heavy fermion problem, Phys. Rev. Lett. **129**, 047601 (2022).

[89] F. Xie, J. Kang, B. A. Bernevig, O. Vafek, and N. Regnault, Phase diagram of twisted bilayer graphene at filling factor $\nu = \pm 3$, Phys. Rev. B **107**, 075156 (2023).

[90] U. Zondiner, A. Rozen, D. Rodan-Legrain, Y. Cao, R. Queiroz, T. Taniguchi, K. Watanabe, Y. Oreg, F. von Oppen, A. Stern, E. Berg, P. Jarillo-Herrero, and S. Ilani, Cascade of phase transitions and Dirac revivals in magic-angle graphene, Nature (London) **582**, 203 (2020).

[91] T. Devakul and L. Fu, Quantum anomalous hall effect from inverted charge transfer gap, Phys. Rev. X **12**, 021031 (2022).

[92] Z. Wang, Y. H. Kwan, G. Wagner, N. Bultinck, S. H. Simon, and S. A. Parameswaran, Kekulé spirals and charge transfer cascades in twisted symmetric trilayer graphene, arXiv:2310.16094.

[93] E. Morissette, J.-X. Lin, D. Sun, L. Zhang, S. Liu, D. Rhodes, K. Watanabe, T. Taniguchi, J. Hone, J. Pollanen, M. S. Scheurer, M. Lilly, A. Mounce, and J. I. A. Li, Dirac revivals drive a resonance response in twisted bilayer graphene, Nat. Phys. **19**, 1156 (2023).

[94] Y. H. Kwan, G. Wagner, N. Bultinck, S. H. Simon, E. Berg, and S. A. Parameswaran, Electron-phonon coupling and competing Kekulé orders in twisted bilayer graphene, arXiv:2303.13602.

[95] L. Huder, A. Artaud, T. Le Quang, G. T. De Laissardiere, A. G. M. Jansen, G. Lapertot, C. Chapelier, and V. T. Renard, Electronic spectrum of twisted graphene layers under heterostrain, Phys. Rev. Lett. **120**, 156405 (2018).

[96] Z. Bi, N. F. Q. Yuan, and L. Fu, Designing flat bands by strain, Phys. Rev. B **100**, 035448 (2019).

[97] T. Soejima, D. E. Parker, N. Bultinck, J. Hauschild, and M. P. Zaletel, Efficient simulation of moiré materials using the density matrix renormalization group, Phys. Rev. B **102**, 205111 (2020).

[98] Y. Saito, J. Ge, K. Watanabe, T. Taniguchi, and A. F. Young, Independent superconductors and correlated insulators in twisted bilayer graphene, Nat. Phys. **16**, 926 (2020).

[99] S. Fang, S. Carr, Z. Zhu, D. Massatt, and E. Kaxiras, Angle-dependent *ab initio* low-energy Hamiltonians for a relaxed twisted bilayer graphene heterostructure, arXiv:1908.00058.

[100] J. Kang and O. Vafek, Pseudomagnetic fields, particle-hole asymmetry, and microscopic effective continuum Hamiltonians of twisted bilayer graphene, Phys. Rev. B **107**, 075408 (2023).

[101] O. Vafek and J. Kang, Continuum effective hamiltonian for graphene bilayers for an arbitrary smooth lattice deformation from microscopic theories, Phys. Rev. B **107**, 075123 (2023).

[102] Z. Dong, M. Davydova, O. Ogunnaike, and L. Levitov, Isospin- and momentum-polarized orders in bilayer graphene, Phys. Rev. B **107**, 075108 (2023).

[103] Z. Liu, E. J. Bergholtz, H. Fan, and A. M. Läuchli, Fractional Chern insulators in topological flat bands with higher Chern number, Phys. Rev. Lett. **109**, 186805 (2012).

[104] T. S. Jackson, G. Möller, and R. Roy, Geometric stability of topological lattice phases, Nat. Commun. **6**, 8629 (2015).

[105] P. J. Ledwith, A. Vishwanath, and D. E. Parker, Vortexability: A unifying criterion for ideal fractional Chern insulators, Phys. Rev. B **108**, 205144 (2023).

[106] P. J. Ledwith, A. Vishwanath, and E. Khalaf, Family of ideal Chern flatbands with arbitrary Chern number in chiral twisted graphene multilayers, Phys. Rev. Lett. **128**, 176404 (2022).

[107] J. Dong, P. J. Ledwith, E. Khalaf, J. Y. Lee, and A. Vishwanath, Exact many-body ground states from decomposition of ideal higher Chern bands: Applications to chirally twisted graphene multilayers, Phys. Rev. Res. **5**, 023166 (2023).

[108] J. Wang, J. Cano, A. J. Millis, Z. Liu, and B. Yang, Exact Landau level description of geometry and interaction in a flatband, Phys. Rev. Lett. **127**, 246403 (2021).

[109] Q. Gao, J. Dong, P. Ledwith, D. Parker, and E. Khalaf, Untwisting moiré physics: Almost ideal bands and fractional Chern insulators in periodically strained monolayer graphene, Phys. Rev. Lett. **131**, 096401 (2023).

[110] D. Varjas, A. Abouelkomsan, K. Yang, and E. J. Bergholtz, Topological lattice models with constant Berry curvature, SciPost Phys. **12**, 118 (2022).

[111] A. Abouelkomsan, Z. Liu, and E. J. Bergholtz, Particle-hole duality, emergent Fermi liquids, and fractional Chern insulators in moiré flatbands, Phys. Rev. Lett. **124**, 106803 (2020).

[112] C. Repellin and T. Senthil, Chern bands of twisted bilayer graphene: Fractional Chern insulators and spin phase transition, Phys. Rev. Res. **2**, 023238 (2020).

[113] P. Wilhelm, T. C. Lang, and A. M. Läuchli, Interplay of fractional Chern insulator and charge density wave phases in twisted bilayer graphene, Phys. Rev. B **103**, 125406 (2021).

[114] J. Wang, S. Klevtsov, and Z. Liu, Origin of model fractional Chern insulators in all topological ideal flatbands: Explicit color-entangled wavefunction and exact density algebra, Phys. Rev. Res. **5**, 023167 (2023).

[115] A. Kumar, R. Roy, and S. L. Sondhi, Generalizing quantum Hall ferromagnetism to fractional Chern bands, Phys. Rev. B **90**, 245106 (2014).

[116] M. Barkeshli and X.-L. Qi, Topological nematic states and non-Abelian lattice dislocations, Phys. Rev. X **2**, 031013 (2012).

[117] M. Barkeshli, C.-M. Jian, and X.-L. Qi, Twist defects and projective non-Abelian braiding statistics, Phys. Rev. B **87**, 045130 (2013).

[118] P. Wilhelm, T. Lang, M. Scheurer, and A. Läuchli, Non-coplanar magnetism, topological density wave order and emergent symmetry at half-integer filling of moiré Chern bands, SciPost Phys. **14**, 040 (2023).

[119] H. Polshyn, Y. Zhang, M. A. Kumar, T. Soejima, P. Ledwith, K. Watanabe, T. Taniguchi, A. Vishwanath, M. P. Zaletel, and A. F. Young, Topological charge density waves at half-integer filling of a moiré superlattice, Nat. Phys. **18**, 42 (2021).

[120] J. Behrmann, Z. Liu, and E. J. Bergholtz, Model fractional Chern insulators, Phys. Rev. Lett. **116**, 216802 (2016).

[121] Y.-F. Wang, H. Yao, C.-D. Gong, and D. N. Sheng, Fractional quantum Hall effect in topological flat bands with Chern number two, Phys. Rev. B **86**, 201101(R) (2012).

[122] M. Trescher and E. J. Bergholtz, Flat bands with higher Chern number in pyrochlore slabs, Phys. Rev. B **86**, 241111(R) (2012).

[123] S. Yang, Z.-C. Gu, K. Sun, and S. Das Sarma, Topological flat band models with arbitrary Chern numbers, Phys. Rev. B **86**, 241112(R) (2012).

[124] A. Sterdyniak, C. Repellin, B. A. Bernevig, and N. Regnault, Series of Abelian and non-Abelian states in $C>1$ fractional Chern insulators, Phys. Rev. B **87**, 205137 (2013).

[125] B. Andrews and G. Möller, Stability of fractional Chern insulators in the effective continuum limit of Harper-Hofstadter bands with Chern number $|C|>1$, Phys. Rev. B **97**, 035159 (2018).

[126] B. Andrews, T. Neupert, and G. Möller, Stability, phase transitions, and numerical breakdown of fractional Chern insulators in higher Chern bands of the Hofstadter model, Phys. Rev. B **104**, 125107 (2021).

[127] Y. H. Kwan, G. Wagner, N. Chakraborty, S. H. Simon, and S. A. Parameswaran, Domain wall competition in the Chern insulating regime of twisted bilayer graphene, Phys. Rev. B **104**, 115404 (2021).

[128] S. Grover, M. Bocarsly, A. Uri, P. Stepanov, G. Di Battista, I. Roy, J. Xiao, A. Y. Meltzer, Y. Myasoedov, K. Pareek *et al.*, Chern mosaic and Berry-curvature magnetism in magic-angle graphene, Nat. Phys. **18**, 885 (2022).

[129] C. Tschirhart, M. Serlin, H. Polshyn, A. Shragai, Z. Xia, J. Zhu, Y. Zhang, K. Watanabe, T. Taniguchi, M. Huber *et al.*, Imaging orbital ferromagnetism in a moiré Chern insulator, Science **372**, 1323 (2021).

[130] J. Shi, J. Zhu, and A. H. MacDonald, Moiré commensurability and the quantum anomalous Hall effect in twisted bilayer graphene on hexagonal boron nitride, Phys. Rev. B **103**, 075122 (2021).